Tectonophysics 880 (2024) 230331

Contents lists available at ScienceDirect

Tectonophysics

journal homepage: www.elsevier.com/locate/tecto

Local earthquake tomography of the Aegean crust: Implications for active deformation, large earthquakes, and arc volcanism

P. Ranjan [a,c,*], K.I. Konstantinou [b]

[a] Taiwan International Graduate Program-Earth System Science (TIGP-ESS), Academia Sinica, Nangang District, Taipei City 115, Taiwan
[b] Department of Earth Sciences, National Central University, No. 300, Jhongda Rd., Chungli, Taoyuan 320, Taiwan
[c] Centre for Scientific and Industrial Research (CSIR)-National Geophysical Research Institute (NGRI), Hyderabad, Telangana 500007, India

ARTICLE INFO

Keywords:
Local earthquake tomography
Aegean crust
Hellenic subduction zone
Large earthquakes
Melt fraction
Santorini caldera

ABSTRACT

Three-dimensional velocity models can enable accurate earthquake location, improved seismic hazard assessment, and can enhance our understanding of geodynamic processes. This is particularly true for areas such as the Aegean, where the crust is marked by active volcanoes as well as shear and rift zones, all of which make this region highly heterogeneous. This work describes the application of local earthquake tomography in order to elucidate the crustal structure of the Aegean. We utilized a dataset of 2,135,625 P arrivals and 1,095,515 S arrivals from 178,676 events recorded across 324 stations. Results indicate that the boundary separating the slow V_p from the fast anomalies at 20–40 km depth is well correlated with the Aegean Moho obtained from receiver functions. A slow V_p (−5%) zone at depths >30 km along the Hellenic arc is likely associated with basal underplating that forms the base of the crust. On the other hand, fast V_p and moderate to high V_p/V_s (1.77–1.92) in the upper-middle crust may indicate evolving metamorphic core complexes. Steeply dipping clusters of earthquakes could highlight pathways of fluid migration from the base to the middle/upper crust, albeit more detailed seismological studies are needed to confirm this interpretation. The 3D velocity model can be also utilized in order to investigate the amount of melt fraction beneath active volcanoes and the influence of fluids on the rupture zone of large earthquakes. Our results show a melt fraction between 4 and 10% beneath active volcanoes, with the largest volume of melt present beneath Santorini caldera. The ruptures zones of 10 large earthquakes ($M_w \geq 6.0$), show slow V_p anomalies and moderate to high V_p/V_s (> 1.77), suggesting that these events were likely triggered by weakening of their source zones by fluid activity.

1. Introduction and background

Tomographic images reveal significant differences in the geodynamics of subduction zones. Subduction zones such as Mariana and Tonga are characterized by steeply dipping slabs (> 40°) whereas those along the Andes and western Mexico have nearly flat slab geometry at depths <125 km (Bijwaard et al., 1998; Fukao et al., 2001). Most low dip slabs are overlain by a continental upper plate, which is advancing trenchwards and exhibits back-arc shortening (Lallemand et al., 2005). The Hellenic Subduction Zone (HSZ) in the eastern Mediterranean Sea (Fig. 1) is unique because even though the slab dip is low to moderate (~20-35°) (Papazachos et al., 2000; Papazachos and Nolet, 1997), the overlying plate is under rapid extension (Reilinger et al., 2006; Shaw and Jackson, 2010). As most of the extensional back-arc systems lie at the ocean-ocean plate convergence, they are mostly inaccessible for geophysical studies. Therefore, the geographical characteristics of the Aegean allow investigations into the structural variations and the deformation of an extending plate.

Numerous geophysical observations have provided clues about the extension in the Aegean lithosphere. GPS studies (see Floyd et al., 2010 and references therein) indicate that the Aegean lithosphere moves SW relative to the African plate at 35 mm/yr, much faster than the African-Eurasian convergence rate (10 mm/yr) (white arrowheads in Fig. 1). This SW expansion of the Aegean is attributed to the Mediterranean slab rollback and the westward extrusion of Anatolia (Reilinger et al., 2010; Jolivet and Brun, 2010). Moho depths derived from receiver functions as well as surface wave dispersion show high variability across the Aegean (Endrun et al., 2008; Karagianni et al., 2005; Li et al., 2003; Sodoudi

* Corresponding author at: Centre for Scientific and Industrial Research (CSIR)-National Geophysical Research Institute (NGRI), Hyderabad, Telangana 500007, India.
E-mail address: pratulranjan@ngri.res.in (P. Ranjan).

https://doi.org/10.1016/j.tecto.2024.230331
Received 4 March 2024; Received in revised form 12 April 2024; Accepted 22 April 2024
Available online 24 April 2024

et al., 2006). The thick fore-arc crust (35–45 km) is explained by nappe-stacking and basal underplating of the subducting material (van Hinsbergen et al., 2005; Burchfiel et al., 2018), while the thin (20–30 km) back-arc crust agrees with back-arc extension (Sodoudi et al., 2006). The minimum principal stress axes are roughly aligned parallel to the Hellenic arc (blue arrowheads in Fig. 1), which emphasizes the role of extension in the regional tectonics (Kapetanidis and Kassaras, 2019; Konstantinou et al., 2017). The earthquakes in the Aegean crust mainly exhibit normal-faulting and strike-slip mechanisms with the thrust-faulting earthquakes limited to the fore-arc, in agreement with the extensional tectonics (Andinisari et al., 2020; Bocchini et al., 2018; Shaw and Jackson, 2010). The crustal fast shear wave directions agree with the regional stress pattern in the fore-arc and align with the structural lineations in the back-arc (Konstantinou et al., 2021).

The extending Aegean lithosphere allows upward migration of fluids, which generate induced seismicity and volcanism. The dense spatial clustering and repeating nature of earthquake swarms in the Corinth rift (see for example Duverger et al., 2018) have invoked hypotheses about fluids ascending from a ductile lower crust (Lambotte et al., 2014; Mesimeri et al., 2019; Pacchiani and Lyon-Caen, 2010). Similar fluid-related earthquake clusters have been discovered in northern Greece and along the fore-arc (Becker et al., 2006; Mesimeri et al., 2017; Ruscic et al., 2019). These micro-earthquake clusters produce fractures in the underlying lithology and may help in the nucleation of large earthquakes (Hickman et al., 1995). Fluids released from slab dehydration generate mafic melts in the mantle wedge, which differentiate to progressively more silicic compositions by fractional crystallization, crustal assimilation, magma-mixing, and crystal-mush rejuvenation, eventually producing volcanism (Francalanci and Zellmer, 2019; Konstantinou, 2020). The Southern Aegean Active Volcanic Arc (hereafter called SAAVA) consists of Sousaki, Aegina-Methana-Poros, Milos, Christiana-Santorini-Kolumbo, and Kos-Yali-Nisyros volcano groups. Volcanic activity along the SAAVA started in the late Miocene coeval with the slab rollback and crustal extension (Fytikas and Vougioukalakis, 2005). Evidences of fluid migration also exist within metamorphic core complexes (MCCs) that are exhumed from middle to lower crust along low-angle detachments. (Huet et al., 2011). Numerical models suggest that during exhumation, the MCCs exhibit ductile behavior and may undergo partial melting (Tirel et al., 2013), which is evidenced by intrusions of granitoids across the Cyclades (Rabillard et al., 2018).

Tomography studies in the Aegean have imaged the deeper HSZ structure (> 50 km) and the average properties of the crust. Images of the geometry of the subducting slab using local and teleseismic earthquakes (Blom et al., 2020; Gesret et al., 2011; Papazachos and Nolet, 1997; Piromallo and Morelli, 2003; Spakman et al., 1988) indicate that the slab has a shallow dip (20°) in the western part, while it steepens in the east (35°) (Fig. 1). Trench-parallel and trench-perpendicular slab tears are observed in the form of fragmented high velocity anomalies at 150–250 km depth at the western and eastern termination of the HSZ (Hansen et al., 2019; Özbakir et al., 2020; Govers and Fichtner, 2016; Kassaras et al., 2020). Detailed images of the western HSZ have helped identify low velocity zones above the slab (90–120 km), which correspond to the basalt-eclogite transition, indicating partial melting in the upper mantle (Halpaap et al., 2018; Pearce et al., 2012; Suckale et al., 2009). Around these depths, high attenuation zones and high scattering strength have been located in the back-arc (Ranjan et al., 2019; Ventouzi et al., 2018). P-wave anisotropic tomography indicates fast directions oriented along N-S/NNE-SSW, consistent with the extensional direction of the Aegean plate (Wei et al., 2019). As an average over crustal depth, localized high scattering attenuation and intrinsic attenuation are observed in both the fore-arc and the back-arc (Ranjan and Konstantinou, 2020). On the other hand, tomographic images of the crustal

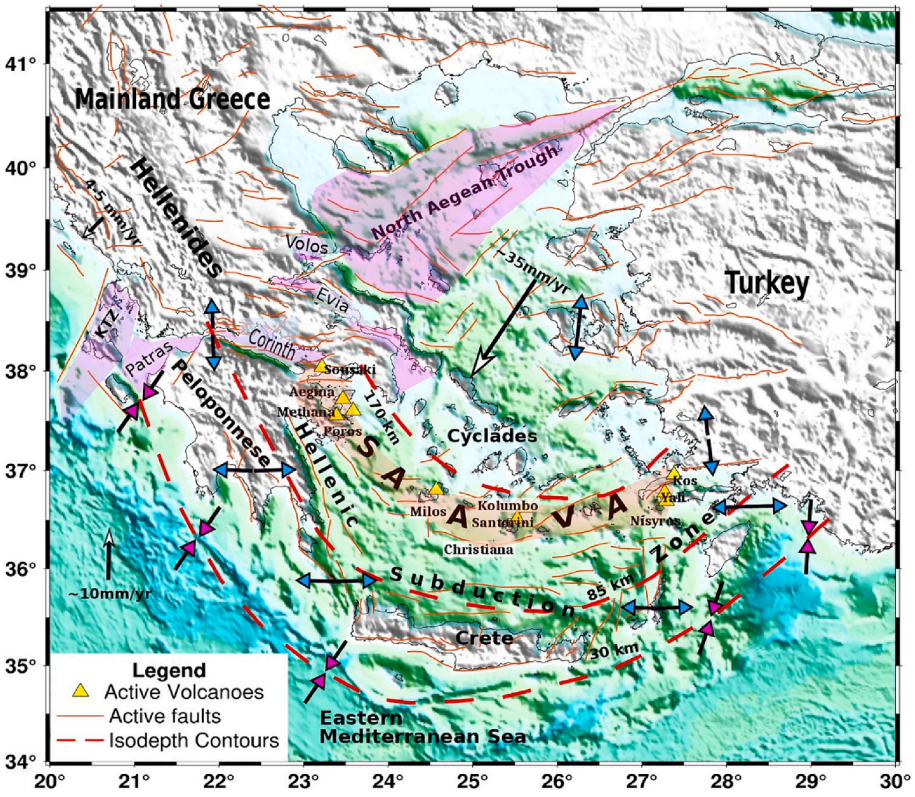

Fig. 1. Topographic and Bathymetric (ETOPO1: Amante and Eakins, 2009) map of the Aegean. The pink patches indicate the major rift/shear zones in the Aegean. The orange patch indicates the southern Aegean Active Volcanic Arc (SAAVA). The isodepth contours are shown with dashed red line (Papazachos et al., 2000). Arrows with purple heads (compression) and blue heads (extension) indicate the regional stress field (Konstantinou et al., 2017). White arrowheads indicate the GPS derived convergence rate. The active faults are taken from the GreDASS database (Caputo et al., 2013). KTZ stands for Kefalonia Transform Zone and SAAVA stands for Southern Aegean Active Volcanic Arc. (For interpretation of the references to colour in this figure legend, the reader is referred to the web version of this article.)

structure of the Aegean mainly exist at the rift zones or near the active volcanoes (Heath et al., 2019; Karakonstantis et al., 2019; Latorre et al., 2004; Papadimitriou et al., 2018).

Because the majority of large earthquakes in the Aegean occur at crustal depths (5–25 km), a detailed 3D velocity model of the crust is needed in order to understand the processes causing these earthquakes and to verify hypotheses about crustal deformation. In this study, we use 10 years (2010−2020) of local earthquake data from the permanent seismic network and from two temporary network deployments (during 2002–2007) in Greece in order to perform seismic tomography in the Aegean using P and S phase travel times. We generate a refined 3D crustal velocity model, which is mostly resolved down to 40 km depth, and would help in the accurate relocation of past and future earthquakes. We begin by compiling the travel time datasets for P and S phases from 194,118 earthquakes recorded by 324 stations in total. Using this dataset and an initial 1D model, we perform model optimization to obtain the reference 1D velocity model and invert for the 3D velocity anomalies using the package LOTOS-12 (Koulakov, 2009). The 3D V_p anomalies, absolute V_p, and V_p/V_s thus obtained, improve our understanding of the composition and the strength of the crust, allow estimation of the melt fraction beneath the active volcanoes, and provide clues about the nucleation process of major earthquakes in the Aegean.

2. Local earthquake travel time tomography

2.1. Travel time data

The initial travel time dataset consisted of 2,661,376 P arrivals and 1,505,187 S arrivals from 194,118 earthquakes recorded across 324 seismic stations. The bulk of the seismic stations belong to three major networks (Fig. 2a):

(1) Hellenic Unified Seismic Network (HUSN) consisting of 211 broadband seismic stations, 14 short-period seismic stations, and 109 strong motion stations from the National Observatory of Athens (1997) (HL), the Aristotle University Of Thessaloniki Seismological Network (1981) (HT), the University of Athens (2008) (HA), the University of Patras (2000) (HP), the Technological Educational Institute of Crete (2006) (HC), and the Institute Of Engineering Seismology and Earthquake Engineering (ITSAK, 1981 HI) for January 2010–April 2020. These networks consisted of 226 unique stations and their data covered the period between January 2010 and April 2020, with magnitude of completeness (Mc) ~ 1.5–2 (D'Alessandro et al., 2011).

(2) Exploring the Geodynamics of Subducted Lithosphere Using an Amphibian Deployment of Seismographs network (EGELADOS Z3) consisting of 56 broadband seismic stations, complemented with 7 short-period seismic stations from the GeoForschungsNetz network (GEOFON GE) and 1 broadband seismic station from the Mediterranean Network (MedNet MN) (Friederich and Meier, 2008) during November 2005–January 2007. These networks consisted of 53 unique stations and their data covered the period between November 2005 and January 2007, with M_c ~ 2 (Brüstle, 2013).

(3) CYClades Seismic NETwork (CYCNET ZZ) consisting of 22 broadband seismic stations (Meier et al., 2004) for September 2002 to September 2005. From this network 20 unique stations were used and the data covered the period between September 2002 and September 2005, with M_c ~ 2 (Brüstle, 2013).

A smaller number of stations was also used for the period between January 2010–April 2020 from neighboring/local seismic networks and strong motion networks, which are listed below:

- 14 broadband/short-period stations from the seismograph network of Corinth Rift Laboratory (CL) (Corinth Rift Laboratory Team And RESIF Datacenter, 2013).
- 3 broadband stations from the Mediterranean network (MedNet MN) (Boschi et al., 1991).
- 3 broadband/short-period stations from the Kandili Observatory and Earthquake Research Institute (KOERI) seismic network (KO) (Cambaz et al., 2019).
- 4 strong motion stations from the Euroseistest strong motion network (EG) (Pitilakis et al., 2013).

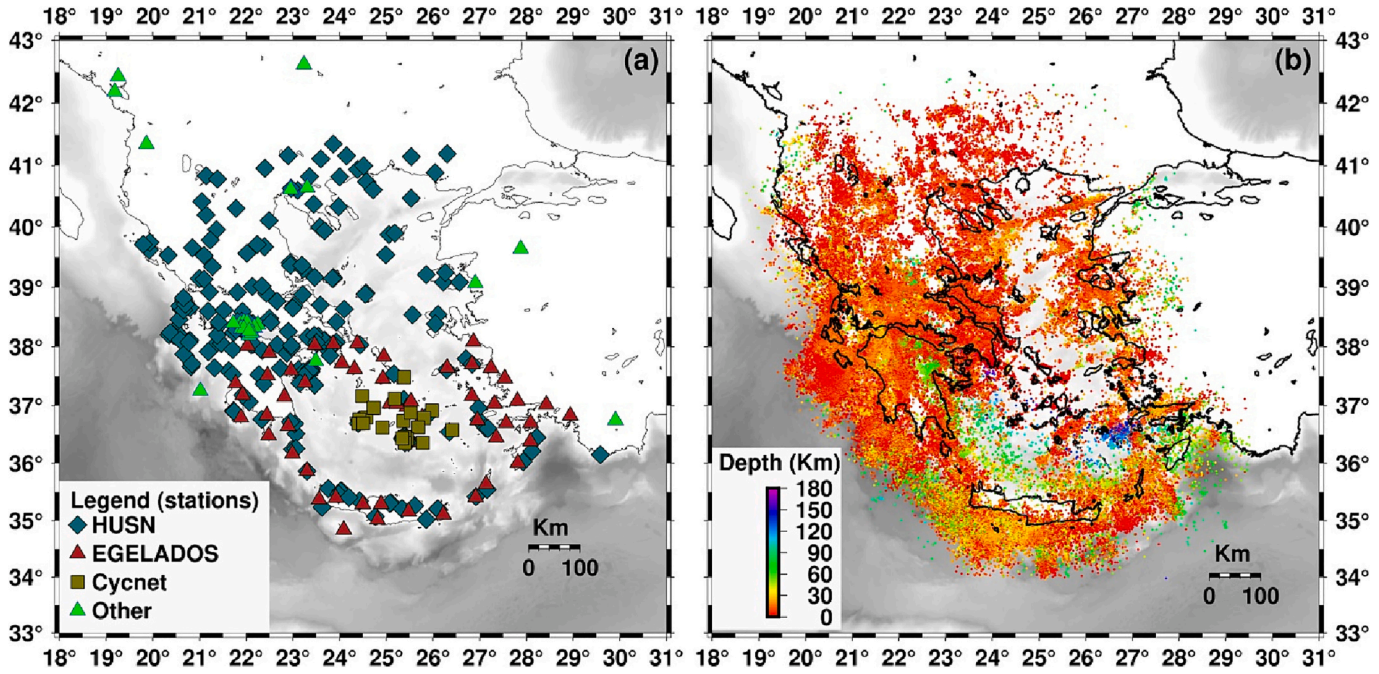

Fig. 2. (a) Stations used in this study from both temporary (EGELADOS and Cycnet), permanent (HUSN), and Other seismic networks (CL, MN, KO, EG, ME) (b) Initial location of the events using the reference 1D velocity model.

- 1 broadband station from the Montenegrin Seismic Network (ME) (Sector For Seismology, 1982).

The spatial distribution of events recorded by stations from the aforementioned networks is shown in Fig. 2b. Most events are located within the top 40 km depth, which corresponds to the maximum crustal depth across the region (Sodoudi et al., 2006). <1% of the events occurred at larger depths (see also Fig. S1), mainly along the SAAVA (Fig. 2b). These events helped increase the ray coverage close to the crust-mantle boundary (see section 2.2.3), allowing improvement in the spatial mapping of velocity anomalies at such depths.

We manually picked the P and S phases from the EGELADOS and CYCNET events while picks from the HUSN events are publicly available from the National Observatory of Athens (NOA) website. The arrival times dataset provided by NOA also contained picks from other neighboring/local broadband as well as strong-motion seismic stations (HC, CL, MN, KO, and EG networks). The NOA picks are first determined automatically and then are visually inspected by analysts, who label them from P_0 to P_4 and S_0 to S_4 based on their quality (0 is the best and 4 is the worst). These picks were assigned Gaussian errors with means 0.05–0.25 s with 0.05 s as a step increment from quality 0 to quality 4. Picks from EGELADOS and CYCNET were assigned a Gaussian error with mean 0.05 s after visual inspection. The station listing was obtained from the European Integrated Data Archive (EIDA) web portal at NOA (http://eida.gein.noa.gr/webdc3/).

2.2. Inversion algorithm and resolution tests

In this study, we use the tomographic inversion package LOTOS-12 (LOcal TOmography Software) developed by Koulakov (2009) to invert for 3D P and S velocity models. LOTOS performs simultaneous inversion of the P and S travel time residuals to obtain 3D velocity anomalies with respect to the reference 1D velocity model. The algorithm starts with a tabulation of theoretical travel times calculated between all pairs of events and receivers using a reference 1D velocity model. The events are then relocated by optimizing a goal function containing the travel time residuals, by searching over coarse to fine grids successively. Then, the events are relocated in 3D using the ray-bending technique (Um and Thurber, 1987), which provides the spatial location of ray paths for each arrival, while optimizing the same goal function using the gradient method. In proportion to the density of ray paths, nodes are installed in 3D (more nodes at higher ray density locations) creating a parameterization grid. Then, the partial derivative of the travel time residual for each ray is calculated with respect to the velocities (V_p and V_s) at all nodes as well as the associated event hypocenter coordinates, origin time, and the station corrections. After that, the partial derivatives along with the damping and smoothing blocks are combined in the form of a matrix, which is inverted for the velocity anomalies as well as for the event locations using the LSQR algorithm (Paige and Saunders, 1982). Next, for several iterations, the events are located in 3D using the new 3D velocity model, new partial derivatives are calculated, and inverted for new velocity anomalies to the point where average travel time residuals do not change significantly. Taking the ratio of the final 3D V_p and V_s models, the 3D V_p/V_s is deduced.

2.2.1. Reference 1D velocity model estimation

As travel time residuals change depending on the 1D model, we considered two different initial models for reference 1D model optimization: the original IASPEI model (Fig. 3a, skyblue colors)and the original Brüstle model (minimum 1D model for southern Aegean, Brüstle, 2013) (Fig. 3a, light green colors). All the events were relocated using the probabilistic earthquake location algorithm NonLinLoc (Lomax et al., 2000) with the above two initial 1D models in order to recalculate the travel times. After location, the arrival phases with large residuals (> 1.5 s) were removed, as such large residuals are unrealistic for local earthquakes, even when using very different 1D velocity models. Only the events with eight or more phases were kept and the arrival times were converted to travel times.

To determine the reference 1D velocity model, we initially used the LOTOS optimization scheme (Koulakov, 2009) with both the original IASPEI and the original Brüstle models. One thousand events with the largest number of phases, best azimuthal coverage and uniform spatial distribution were selected for velocity model optimization using each of the original IASPEI and the original Brüstle models. Maximum

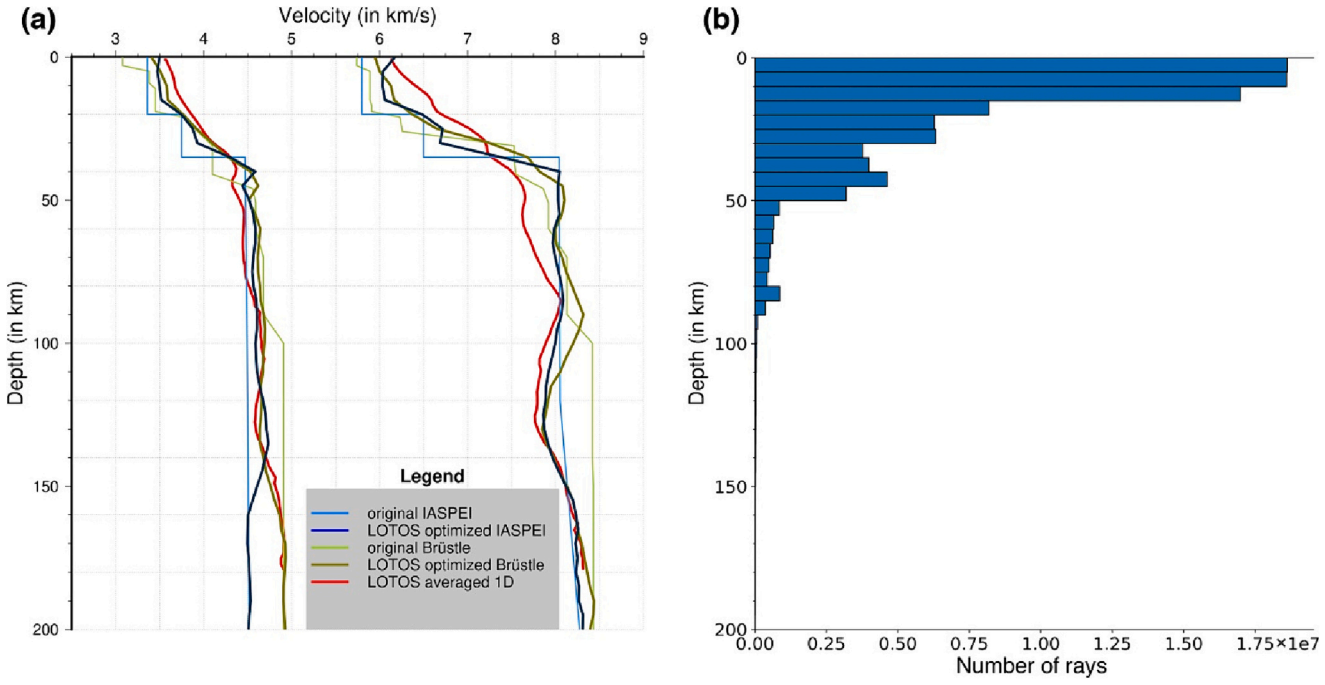

Fig. 3. (a) All 1D velocity models that were tried as starting models. Red lines represent the reference velocity model (LOTOS averaged 1D) finally used as the starting model for tomographic inversion. (b) Distribution of depth penetration of ray paths after five iterations of tomographic inversion. (For interpretation of the references to colour in this figure legend, the reader is referred to the web version of this article.)

perturbations of 5%, 10%, and 15% around each of the original IASPEI and the original Brüstle models were used to generate 90 different starting models in each case. Each of these starting models were fed into the optimization scheme, and the optimized models with the smallest residuals were averaged separately to obtain the LOTOS optimized IASPEI (Fig. 3a, dark blue colors) and the LOTOS optimized Brüstle (Fig. 3a, dark green colors) models respectively. However, we observed that both of these optimized models exhibited the same sharp velocity contrasts as those found in the original Brüstle and IASPEI models (Fig. 3a). We tried tuning the optimization parameters, but the results did not change significantly. This suggests that the models obtained from the LOTOS optimization scheme may have a strong bias towards the initial model.

To overcome this bias, we performed the 3D tomographic inversion using the optimized Brüstle model (Fig. 3a, dark green colour) and averaged the velocities in horizontal sections at each depth level to obtain an average 1D velocity model. Then, using this model as the starting one, we relocated all 194,118 events, re-performed the 3D tomographic inversion, and obtained a new average 1D velocity model. This process was repeated until the average 1D velocity models did not show significant variation. Our approach is essentially the same as that of García et al. (2019) for 1D velocity model optimization. During these runs, the weights for different optimization parameters were left unchanged and were derived from the standard values in the LOTOS manual, so that the optimization parameters do not significantly bias the averaged 1D models. Finally, the stable average 1D velocity model, LOTOS averaged 1D (Fig. 3a (red colour)) was used for tomographic inversion. All the events were again relocated using NonLinLoc with this 1D model, while phases with large residuals ($>$ 1.5 s) were rejected, and only events with eight or more phases were kept, obtaining the travel time dataset for 3D tomographic inversion. This relocation with NonLinLoc was performed to adjust the origin time of the events based on the LOTOS averaged 1D model and recalculate the travel times. During the LOTOS locations using the averaged 1D model, several events having $>$30% bad phases (travel times with residuals $>$1 s) were rejected, and we were left in the final dataset with 178,676 events consisting of 2,135,625 P and 1,095,515 S arrivals for the tomographic inversion. Equal weights were assigned to P and S travel times, during the inversion.

2.2.2. Optimization for inversion parameters and 3D inversion

The LOTOS 3D inversion algorithm consists of weights for amplitude damping, smoothing, factors for event relocation term (i.e. horizontal, vertical, and origin time shift), and for the station corrections. We derived all the weights (except those for station corrections) using the maximum curvature point of the U-curve (Watkins et al., 2018 and references therein) which is a plot of the sum of normalized RMS residuals and the normalized model perturbation versus the different weights (Fig. S3). We optimized each parameter weight by running the tomographic algorithm 5–8 times for three iterations. The three iterations were performed so that the 3D velocity model becomes stable, and the residuals converge to a stable value for each set of inversion parameters. We began by assigning near zero weights for all parameters and sequentially optimized the damping, smoothing, and source (event) shift weights. The damping weights of 8 for P and 6 for S, smoothing weights of 3 for P and 5 for S, source shift weights of 10 in horizontal and vertical direction as well as in origin time were found to be optimum. Station corrections help to remove artifacts in the shallow 3D velocity model that may be generated by near surface features that lie directly beneath the stations. In our case, different weights for station corrections did not appear to change the recovered shallow model (Fig. S4), therefore, we did not apply any such weights.

We executed the tomographic algorithm for five iterations as it has been observed in several tomographic inversions using LOTOS that the residuals do not change significantly after four iterations (see Koulakov et al., 2019 and references therein). A 10 km $\times$ 10 km $\times$ 5 km spaced grid was used for 3D-location and inversion, where nodes are located based on ray density up to a maximum depth of 180 km corresponding to the deepest earthquakes in the Aegean. In areas with lower number of rays, the distance between the nodes is larger. Four different orientations of the 3D grid were used: 0^o, 22^o, 45^o, and 67^o, and the results were averaged for a robust estimate independent of the grid orientation used. The ray density plots for 0^o and 67^o grids in N-S oriented vertical cross sections are provided in Figs. S5-S8. The elevation information of the stations was also included in the inversion, while the parameterization grid was defined from 5 km above the surface.

The evolution of residuals starting from the averaged 1D model locations using NonLinLoc up to the final 3D locations using LOTOS are shown in Fig. 4. The higher average residuals obtained from LOTOS 1D locations versus NonLinLoc 1D locations is likely due to the differences in the location algorithm (linearized versus nonlinear probabilisitic). All 178,676 events were used for 3D location using LOTOS, which generated a small reduction of average residuals after the first iteration. Subsequently, the joint inversion for the V_p and V_s models and earthquake locations were performed using LOTOS iteratively. The P and S residuals at the end of five iterations are considerably reduced compared to the original NonLinLoc 1D locations or LOTOS 1D locations. The variance reduction and the residuals after each iteration of the tomographic inversion are provided in Table 1. The variance reduction for S residuals is significantly higher than P residuals because of the higher sensitivity of S travel times to velocity anomalies. This observation is not unique to this work and it has also been reported in previous studies (e.g., Koulakov et al., 2019).

We did not have separate Pn and Pg phases in our dataset, since all first arrivals were marked as P phase. The error in event location due to inaccurate phase labels is partly alleviated by using NonLinLoc for initial event locations, which is capable of calculating first arrival travel times in complex media using a finite difference approach (Podvin and Lecomte, 1991). The LOTOS algorithm models the ray paths using the ray-bending technique, which is also capable of modeling ray paths for Pn arrivals. For events that are near the Moho, close to real Pn ray paths can be obtained, because the required amount of bending would be small. For events in the mid-crust or shallow crust, Pn is the first arrival only at large distances from the source. At such hypocentral distances, weights used in LOTOS 1D location would weigh down these travel times, excluding many of these arrivals from 3D location. The remaining Pn arrivals that could not be modeled by the ray-bending algorithm likely have large residuals and these are again weighed down significantly during 3D inversion. We do note, however, that they may contribute towards increasing the average residuals. At the end of five iterations, we find that only 1.74% of the total number of ray paths penetrate the depth of 30 km (Fig. 3b), which is the average Moho depth in the Aegean (Sodoudi et al., 2006). We can conclude therefore that possible misidentification of Pn phases as crustal P phases is negligible and cannot bias our inversion results.

2.2.3. Horizontal and vertical resolution tests

We performed two kinds of synthetic checkerboard tests to determine the resolution of the final 3D velocity model: (1) Horizontal resolution tests along selected depth slices (2) Vertical resolution tests along selected depth cross-sections. Checkerboard anomalies of $\pm$ 5% were assigned with respect to the averaged 1D model, with opposite sign of the V_p and V_s anomalies so that the V_p/V_s obtained after division of the two checkerboards shows high and low V_p/V_s values similar to a checkerboard pattern. We defined the checkerboard anomalies from 10 km above zero depth as recommended in the LOTOS manual, to avoid upward ray-bending in case of slow near-surface anomaly. The source-receiver pairs were taken from the fifth iteration of the final 3D inversion. A Gaussian random noise with standard deviation of 0.18 s for P and 0.07 s for S was added to synthetic arrival times based on the variance reduction of residuals observed in the real dataset. After that, the original source locations were erased and the LOTOS algorithm was

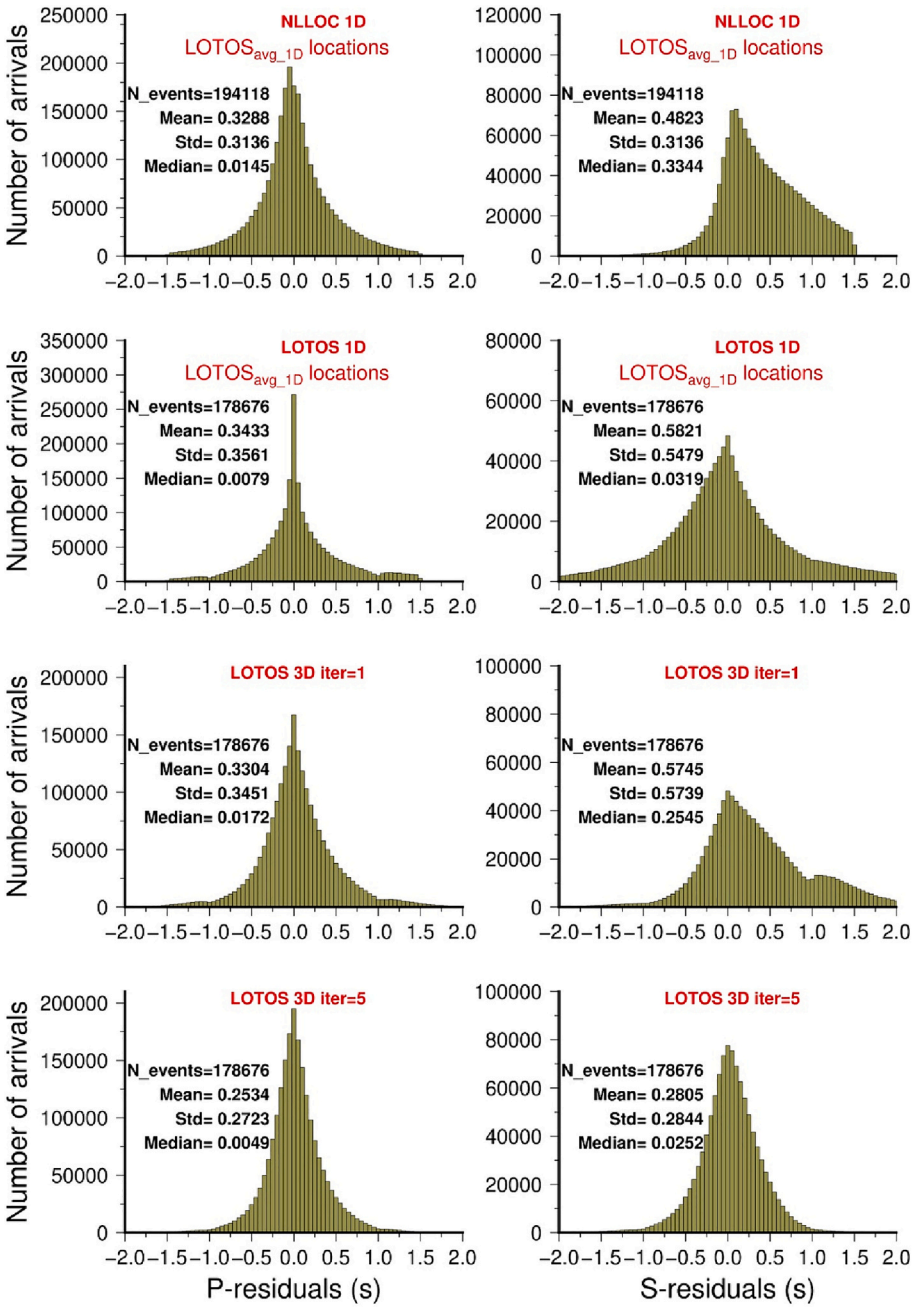

Fig. 4. Evolution of residuals from locations with 1D model using NonLinLoc to locations with 3D model using LOTOS for both P and S trravel times. Note that the histogram shape in the top right panel (NLLOC 1D) is due to the cutoff limit applied to positive and negative residuals for the S travel times.

Table 1
Summary of the residuals after five iterations of the tomographic inversion.

Iteration No.	P Variance Reduction (%)	P average residual (s)	S Variance reduction (%)	S average residual (s)
1	0.00	0.330	0.00	0.574
2	15.09	0.281	44.38	0.320
3	20.87	0.261	48.61	0.295
4	22.50	0.256	50.37	0.285
5	23.30	0.253	51.18	0.280

used for the recovery of the checkerboard anomalies as well as the source locations. The horizontal resolution test results are shown for two anomaly sizes: 30 km × 30 km × 30 km and 50 km × 50 km × 30 km for V_p and V_p/V_s (Figs. 5, 6). The horizontal resolution test results for the S-anomalies and the inverted V_s anomalies in the 0–40 km horizontal slices are provided in the supporting information (Fig. S9, S10).

The synthetic checkerboard tests of the V_p model exhibit broad similarities for both anomaly sizes in the 5–15 km depth slices. The checkerboard pattern is almost fully recovered for the area of central Greece, Peloponnese, gulf of Patras and the area that abuts KTZ (see also Fig. 1). In the areas of northern and NE Greece the pattern seems to be partly recovered at the same depths, and the same is true for the Cyclades and the island of Crete in the southern Aegean. In the 20–40 km depth slices, the pattern with anomaly size of 50 km × 50 km × 30 km is recovered fully or partially in the same areas, however, the anomaly size of 30 km × 30 km × 30 km is fully recovered only in central Greece and the Peloponnese. In large areas of the NE Aegean and between Crete and the Cyclades in the southern Aegean, the pattern for both sizes either cannot be recovered or the shape and amplitude of the anomalies are

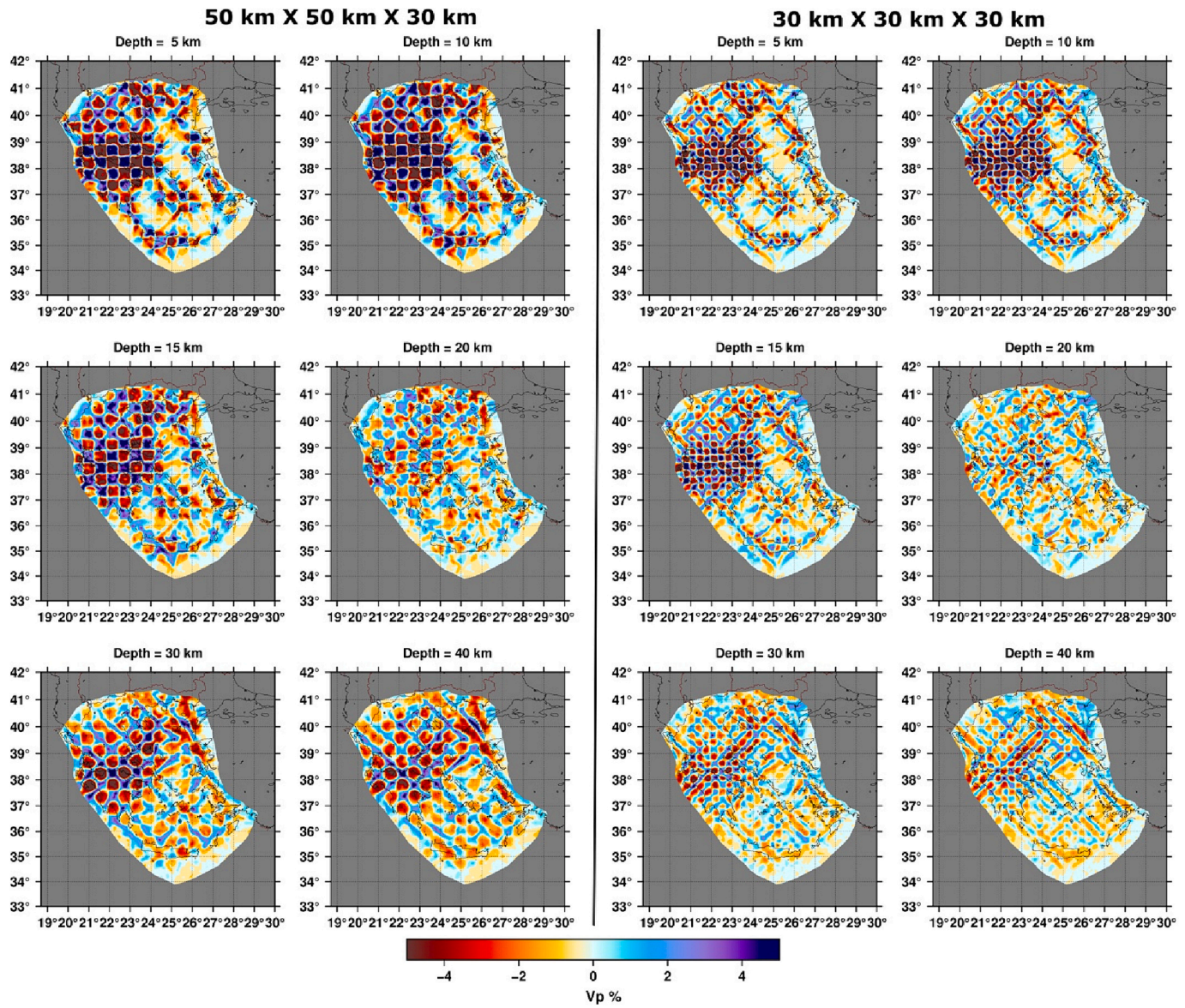

Fig. 5. Results of the horizontal checkerboard tests for P-wave velocity (see text for more details).

severely distorted at all depth slices. The situation is similar in the case of the V_p/V_s checkerboard test, with the difference that in the areas of the southern Aegean the pattern can be partly recovered for all depth slices in the 50 km × 50 km × 30 km anomaly size. Due to the close proximity of anomalies in these checkerboard tests, it is difficult to identify directional distortion of the recovered anomalies. Therefore, we also tested the resolution by performing spike tests (sparse checkerboards) (Rawlinson and Spakman, 2016) with 30 km × 30 km × 30 km anomalies (Fig. S11). Spike tests help identify locations where the shape of the anomaly is not well recovered owing to increased smearing. As in the usual checkerboard tests, spike test results show that the regions in NE and southern Aegean exhibit higher degree of smearing, hence these areas are mostly excluded from further discussion. Overall, good recovery of the spikes with minimum smearing for V_p and V_p/V_s models can be observed for the majority of mainland Greece, Peloponnese and some parts of the Cyclades.

We also compare the shift in source locations during horizontal checkerboard tests (30 km × 30 km × 30 km case) in Fig. S12. The source locations in the 1D model show a large shift (median ~ 8.9 km) from their original positions because the synthetic travel times are calculated in the checkerboard model and they contain random noise. After the five iterations of the tomographic inversion, however, the sources are relocated back in their original positions with much smaller uncertainty (median ~ 2.7 km), minimizing the influence of random error. These plots show that the trade-off between source locations and velocity model estimation does not significantly affect the source relocation accuracy.

For the vertical resolution tests, we chose anomaly sizes of 50 km × 50 km × 50 km, 30 km × 30 km × 30 km, and in some cases 20 km × 20 km × 20 km along selected vertical cross-sections that represent the rupture zones of large earthquakes (see section 4.4). The cross-sections were chosen at locations where both V_p and V_p/V_s show high resolution in the horizontal checkerboard tests (central Greece, Peloponnese, areas that abut KTZ, Crete, volcanoes of SAAVA). Here, we only show the masked cross-sections based on the results of the vertical resolution tests. The vertical resolution test results for these cross-sections are provided in the supporting information (Figs. S13, S14, S15, S16, S17, S18, S19, and S20). In general, these tests indicate good resolution in most parts of the chosen cross-sections for both V_p and V_p/V_s down to 40 km depth (down to 60 km depth in some cross-sections). In summary, we can conclude that our tomographic model in central Greece, Peloponnese, areas that abut KTZ, Crete, and the volcanoes of SAAVA,

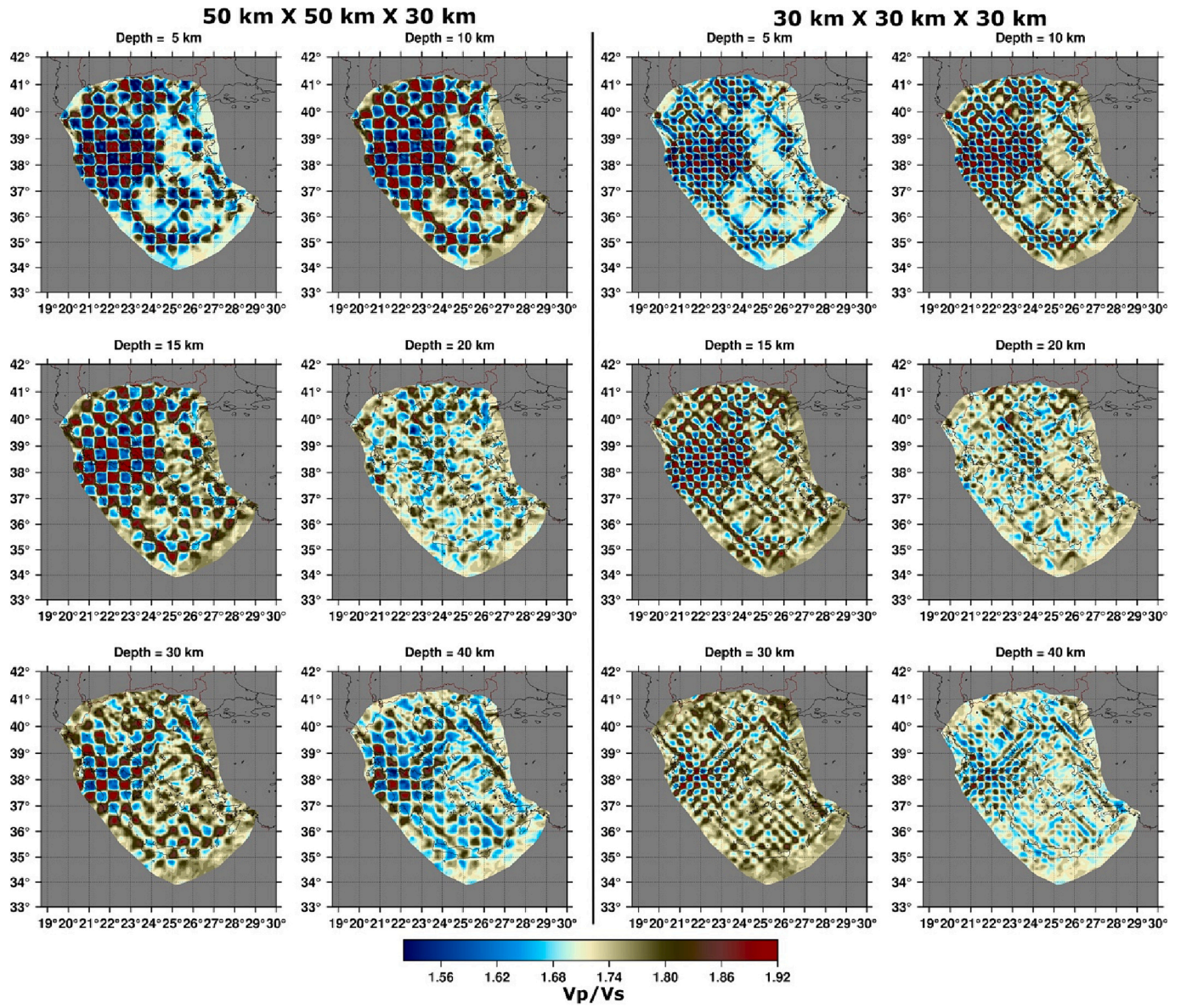

Fig. 6. Results of the horizontal checkerboard tests for V_p/V_s (see text for more details).

exhibits horizontal and vertical resolution in the order of 30 km. Therefore, in the following sections, we will only discuss results from these locations.

2.2.4. *Sensitivity and robustness tests*

In order to check the robustness of the 3D model with respect to errors in earthquake locations, we filtered the original dataset to select the best event in each 10 km × 10 km × 3 km bin. To identify the best events, a score that is the weighted sum of the normalized azimuthal gap (weight = 2), normalized nearest station distance (weight = 2) and the normalized number of phases (weight = 1) was assigned to all the events. Then, in each bin the event with the best score was selected. The scoring technique was used to ensure uniform spatial coverage and the weights were chosen based on relative importance of parameters in source location accuracy (Bondár et al., 2004). After filtering, we obtained 33,821 events, with 501,540 P arrivals and 262,580 S arrivals. The tomographic inversion with the same parameters as the full dataset was run for 5 iterations using this filtered dataset and the results in 5–40 km horizontal slices are shown in Figs. S21, S22. Except for the 5 km slice, all other slices have similar anomalies and V_p/V_s pattern as the results obtained using the full dataset. Even in the 5 km slice, the shape of the anomalies is similar for both the filtered and full dataset, with reduced amplitude in the filtered dataset likely due to fewer ray paths. Therefore, we can conclude that the noise in the arrival times or poorly located events in the full dataset do not significantly affect the final results.

Another robustness test is the odd-even test, where the full dataset is divided into two parts: one containing only the odd numbered events (odd dataset), and another containing only the even numbered events (even dataset). If there is any systematic bias in the full dataset, the results obtained using the odd dataset should differ significantly from those obtained using the even dataset. For both the odd and the even dataset, the results for V_p anomalies and the V_p/V_s appear very similar (Figs. S23, S24). When these results are compared to those obtained using the full dataset, the odd or even dataset results exhibit smaller amplitude, which is likely due to lower density of ray paths in the odd or even dataset.

3. Results

The results of the tomographic inversion for the V_p anomalies in horizontal sections are shown in Figs. 7 and those for the V_s are shown in Fig. S10 for reference. Strong slow (> 5%) V_p anomalies are observed in the Gulf of Corinth from 5 to 20 km depth and in the KTZ at 15 km and 20 km depths. From 20 km onwards, a strong slow V_p anomaly is observed extending all along the fore-arc. Moderately slow (< 5%) V_p anomalies also appear in the Cyclades and eastern Greece in 0–20 km depth range. Fast V_p anomalies are observed over most of the Cyclades and the Aegean Sea in 30–40 km sections. Beneath the SAAVA, Christiana-Santorini-Kolumbo and Kos-Yali-Nisyros exhibit moderately

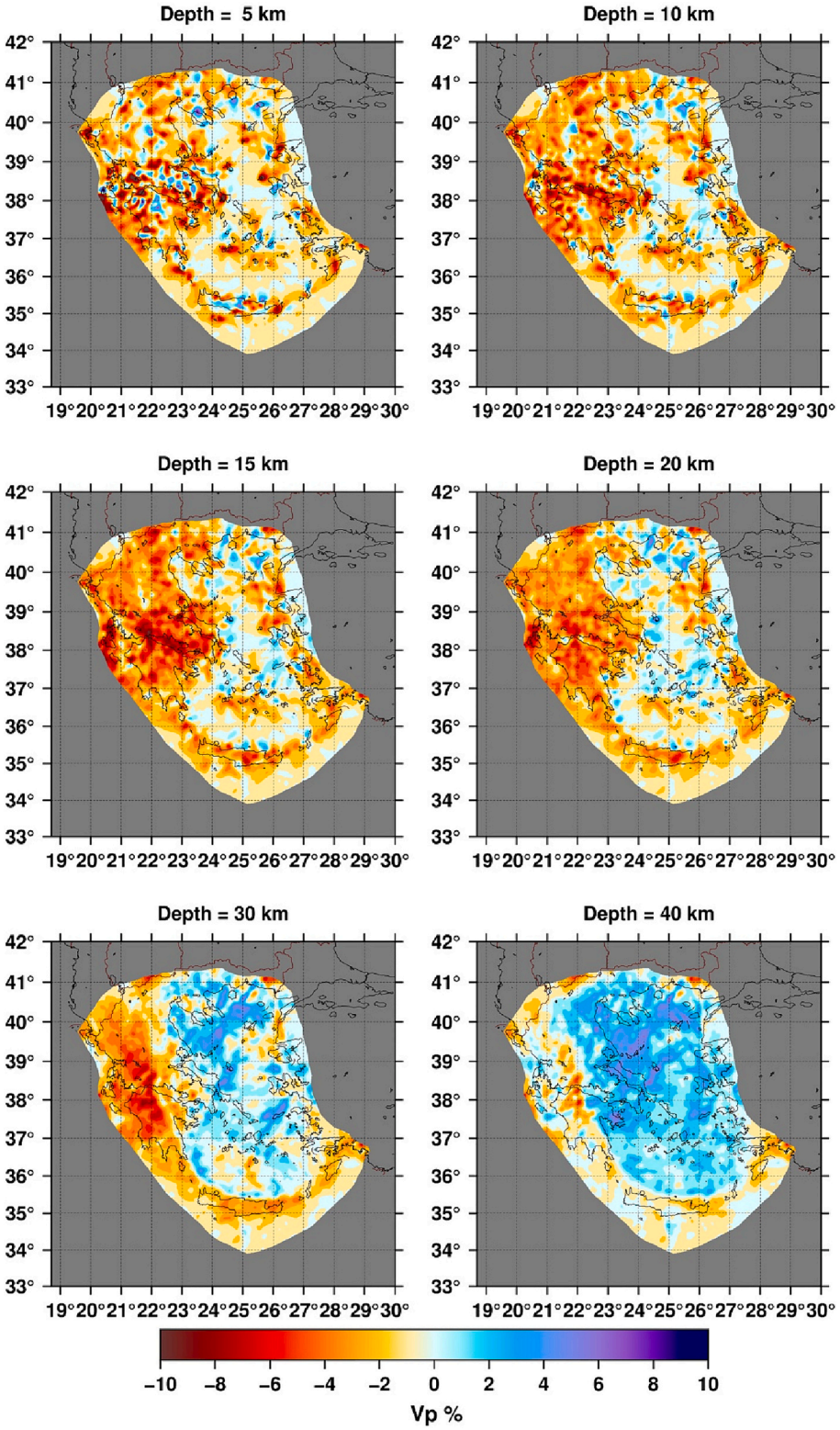

Fig. 7. P-wave anomalies after tomographic inversion are shown in 6 horizontal depth sections: 5 km, 10 km, 15 km, 20 km, 30 km, and 40 km. The regions outside the coverage of seismic networks in the Aegean have been masked.

slow V_p anomalies down to a depth of 30 km. Poros-Methana-Aegina shows alternating moderately fast and slow anomalies down to 30 km depth and fast anomalies afterwards (see also section 4.3 for more details).

The results for V_p/V_s are shown in Fig. 8 with the mean value in the colour scale set to 1.77 corresponding to the average Poisson's ratio for a 40 km thick continental crust (Christensen, 1996). High V_p/V_s (1.86–1.92) is observed around the KTZ, NW Peloponnese, the gulfs of Patras and Corinth, as well as the gulf of Gökova at shallow depths (5–15 km). At 10 km depth, the KTZ and the westernmost gulf of Corinth show extremely high Vp/Vs (> 1.92). At 15 km depth, the average V_p/V_s across the region increases close to 1.80. Large zones of high V_p/V_s are

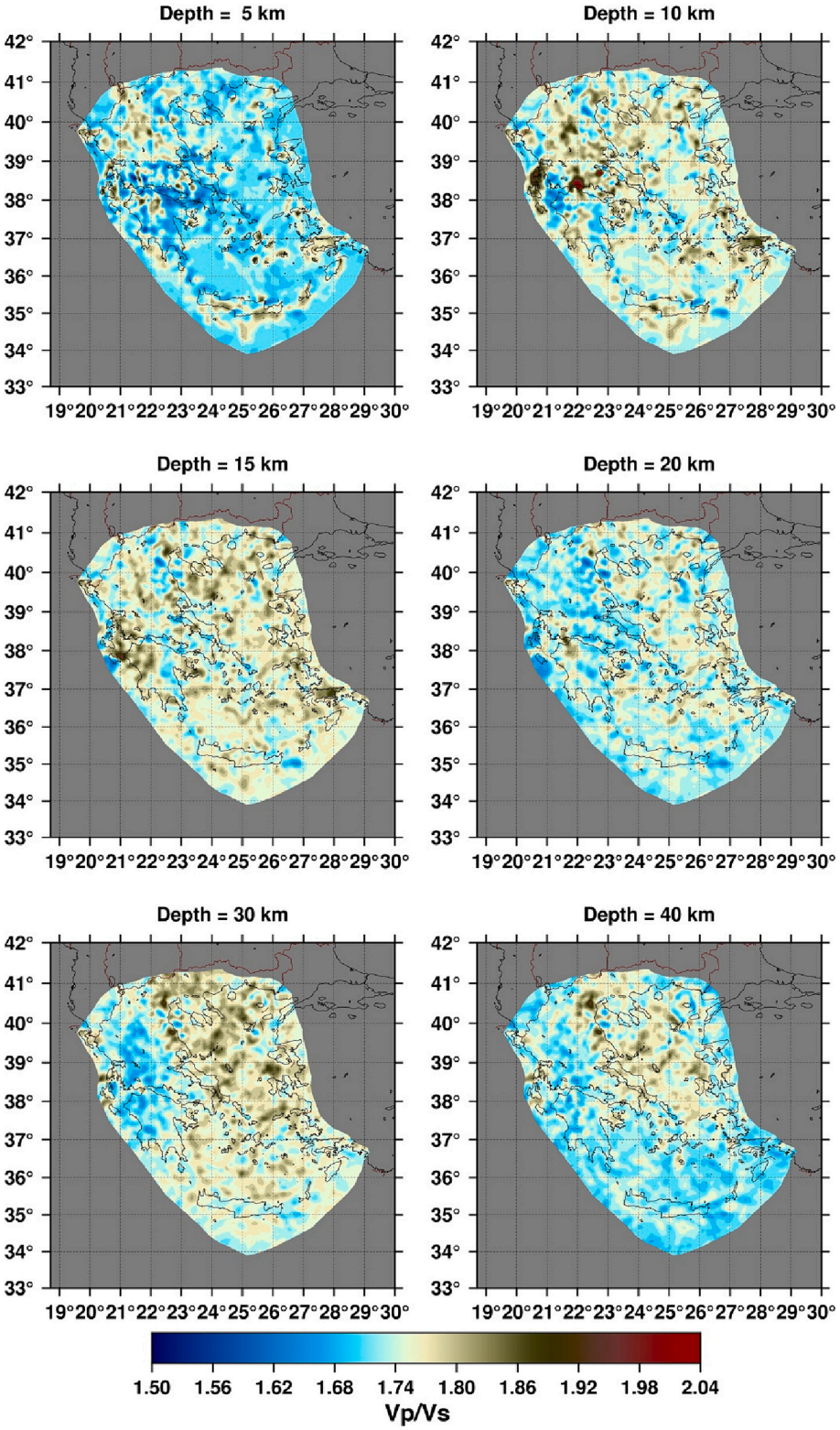

Fig. 8. V_p/V_s ratio after tomographic inversion is shown in 6 horizontal depth sections: 5 km, 10 km, 15 km, 20 km, 30 km, and 40 km. The regions outside the coverage of seismic networks in the Aegean have been masked.

observed in NW Peloponnese at 15 km depth and the Saronikos gulf at 10–15 km depth. Moderately high V_p/V_s (1.80–1.86) is also observed south of Crete down to 15 km depth. After 15 km depth, high V_p/V_s zones shift towards the back-arc. Extremely low V_p/V_s (< 1.60) is observed across the gulfs of Patras, Corinth, Evia, and Volos at 5 km depth. In the gulf of Patras, extremely low V_p/V_s extends down to 10 km depth. Beyond 15 km depth, V_p/V_s values become moderately low (1.60–1.77) through most of the Peloponnese and mainland Greece excluding the back-arc. Among the SAAVA volcanoes, high V_p/V_s is observed between 5 and 15 km depth below the Poros-Methana-Aegina group, while Sousaki and Milos do not show consistently high V_p/V_s values. Santorini-Kolumbo show high V_p/V_s in 5–10 km range and high V_p/V_s in 20–30 km range is observed beneath Christiana. The Kos-Yali-Nisyros group shows moderately high V_p/V_s (1.77–1.86) in the top 5 km and high V_p/V_s (> 1.86) at 10–15 km depth (see also section 4.3 for more details).These results are broadly consistent with previous geophysical studies of the Aegean crustal structure. Estimates of intrinsic and scattering attenuation zones in the crust show good correlation with the zones of high and moderately high V_p/V_s at shallow depths (< 20 km) along the gulf of Corinth, Crete and the back-arc (Ranjan and Konstantinou, 2020). High V_p/V_s zones at larger depths (> 20 km) overlap with the region of higher scattering inhomogeneities

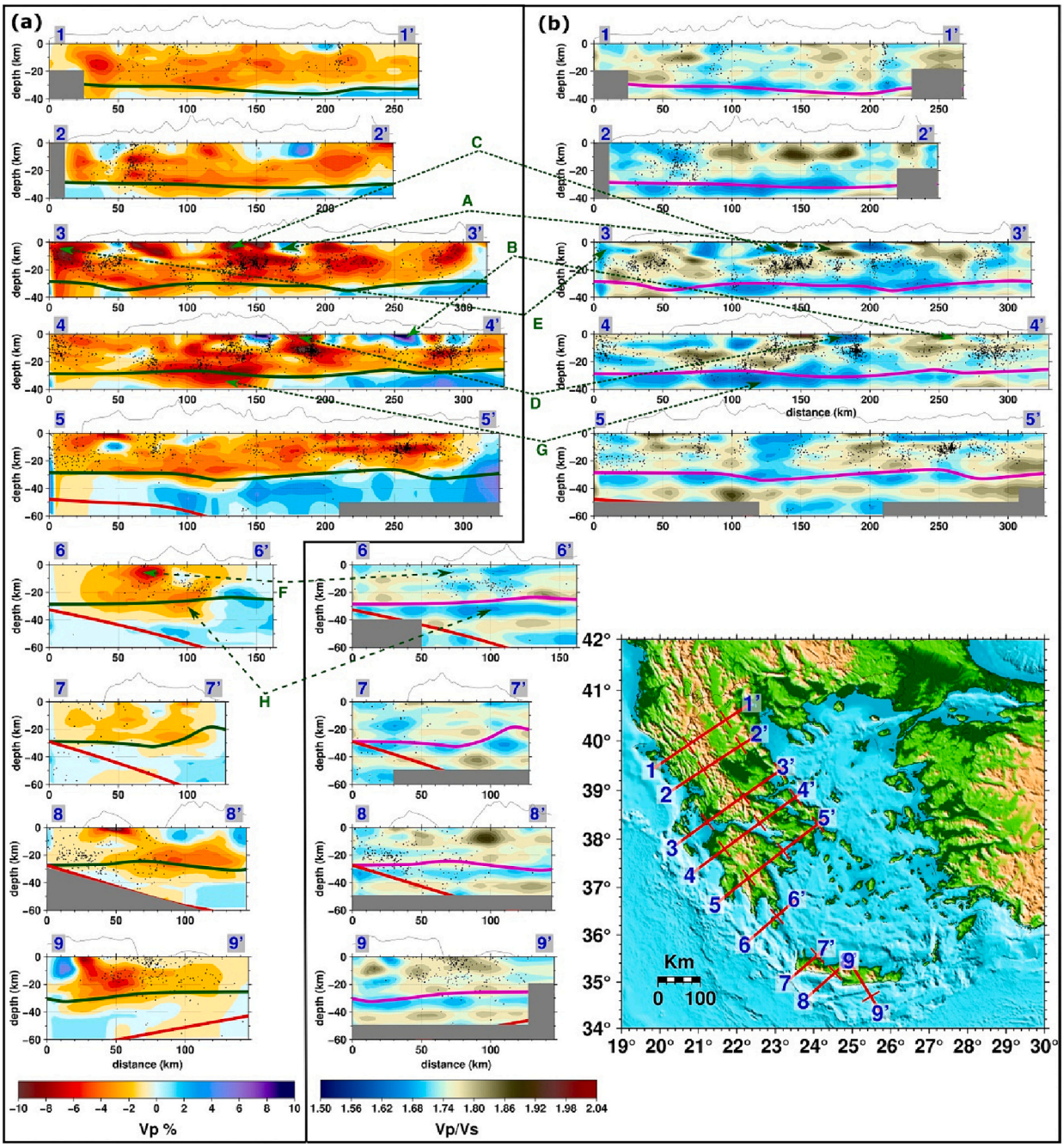

Fig. 9. (a) V_p anomalies, and (b) V_p/V_s ratios along the Hellenic arc in vertical cross-sections numbered from 1 to 1′ to 9–9′. All cross-sections are oriented SW-NE except 9–9′, which is oriented NE-SW. Cross-sections 1–1′ to 4–4′ show depths up to 40 km while later cross-sections extend up to 60 km. Both Aegean Moho (green line in (a) and magenta line in (b)) and the African Moho (red line) derived from Sodoudi et al. (2006) are outlined. The small black dots in each cross-section indicate relocated earthquakes, within 5 km of its strike. Areas that were not resolved in vertical resolution tests are masked with grey rectangles. Specific anomalies are marked with bold-faced capitalized letters. (For interpretation of the references to colour in this figure legend, the reader is referred to the web version of this article.)

in the back-arc, even though direct correlation is not always expected (Ranjan et al., 2019). Local earthquake tomography of the western Corinth rift indicates high V_p/V_s zones in 5–10 km depth range (Latorre et al., 2004); however, our results show high V_p/V_s only in the 10 km depth section. Among the volcanic centers, high V_p/V_s zones beneath the Poros-Methana-Aegina group in 10–20 km depth range were also observed in a recent local earthquake tomography study (Karakonstantis et al., 2019). Local earthquake tomography as well as active seismic source imaging of the Christiana-Santorini-Kolumbo group indicates low V_p anomalies in the upper 5–6 km beneath Santorini (Dimitriadis et al., 2010; Hooft et al., 2019; McVey et al., 2020). Even though our resolution is lower than these active source experiments, we observe low V_p and high V_p/V_s beneath Santorini and Kolumbo in the horizontal section at 5 km depth. At Kos-Yali-Nisyros, we observe a low V_p and moderately high V_p/V_s zone beneath and SW of Nisyros down to 15 km depth as has been also found in a previous tomographic study of this region (Papadimitriou et al., 2018).

4. Discussion

4.1. Structural variations of the Aegean crust

The seismic Moho by definition is the boundary separating the crust and the upper mantle and is marked by a V_p change from 6.5 to 7.1 km/s to 7.6–8.1 km/s (Carbonell et al., 2013). We overlay the vertical cross-sections with the Aegean Moho boundary derived from a previous receiver function study (Sodoudi et al., 2006) for comparison. The Aegean Moho boundary roughly follows the V_p anomaly transition from slow to fast anomaly at depths >20 km (Figs. 9, 10). This feature is clearly observed along the green colour line in sections 4–4′ (horizontal distance of 150 km onwards), 5–5′, 2–2′ (horizontal distance of 0–70 km and 180+ km). The Moho estimates using both receiver functions and surface wave dispersion indicate a thicker crust beneath the northern Hellenides (40 km) compared to the south (30 km) that gradually thins outwards from the center in *E*-W direction (Sodoudi et al., 2006; Endrun et al., 2008; Karagianni et al., 2005). We also observe a thicker crust beneath the northern Hellenides and a gradual decrease away from the central part (Figs. 9, 10: 1–1′ to 4–4′). At a few locations where the slow-fast V_p boundary is not observed, V_p anomalies may not be fully resolved (0–50 km along the cross-sections in Fig. 9a: 1–1′ to 4–4′). It is also important to note that the Moho boundary inferred from receiver functions is an interpolation between single station estimates, hence at locations where the slow V_p anomaly appears to extend deeper than this boundary it is likely that the crust there may be thicker.

Zones of fast and slow V_p anomalies are observed within the crust in all cross-sections along the Hellenic arc (Fig. 9a). Fast V_p anomalies indicate more mafic concentration while slow V_p anomalies imply greater silicic composition. Several fast V_p anomalies in the upper crust also have moderately high to high V_p/V_s (Fig. 9: features A and B) and an absolute V_p in the range of 6.5 to 7.0 km/s (Fig. 10), that is consistent with middle to lower crustal velocities (Christensen and Mooney, 1995; Christensen, 1996). The slow V_p anomalies have both high and low V_p/V_s and they show a range of different absolute velocities. Very slow V_p anomalies at shallow depths (< 10 km) are observed in the basin areas such as gulf of Corinth, gulf of Patras (Fig. 9: Features C and D) and the western fore-arc (Fig. 9: Features E and F). These regions also have absolute $V_p \leq 6.0$ km/s (Fig. 10) and low V_p/V_s (Fig. 9b), which indicates clear association to sedimentary assemblages (Johnston and Christensen, 1992). Slow V_p anomalies at the base of the Aegean crust also exhibit moderately low to extremely low V_p/V_s, however, their absolute V_p is high (6.6–7.3 km/s).

Fast V_p anomalies observed at upper crustal levels (Features A and B) might be associated with the metamorphism of rocks accreted from the subducting crust as a result of nappe stacking of continental and oceanic fragments (van Hinsbergen et al., 2005). The absolute velocities in the range 6.5–7.0 km/s and high V_p/V_s suggest that these are mafic metamorphosed rocks, based on laboratory measurements at high pressures (Christensen and Mooney, 1995). This inference is also supported by empirical relations between V_p and V_p/V_s for mafic or Ca-rich crustal rocks (Brocher, 2005), that indicate V_p/V_s between 1.84 and 1.85 for P velocities in the range of 6.5–7 km/s. Therefore, features A and B exhibit similar properties as the mafic or Ca-rich crustal rocks. Due to the abundance of outcrops of mafic rocks (Blueschists, Greenschists, Ambhibolites) and Ca-rich rocks (marbles) of metamorphic type across the Aegean (Jolivet and Brun, 2010), the features A and B in the upper crust may likely be of metamorphic type. Lithological units accreted from the subducting crust by nappe stacking (van Hinsbergen et al., 2005) underwent high-P, low-T metamorphism and were later overprinted by retrograde metamorphism during exhumation to form metamorphic core complexes (MCCs) (Jolivet et al., 2013; Ring et al., 2010). The outcrops of MCCs are found mainly across the Cyclades and Crete (Jolivet and Brun, 2010), however, extension of the metamorphic basement rocks is still ongoing across the Aegean. Therefore, it is possible that the mafic metamorphic rocks at upper crustal depths observed in features A and B may share similar evolution as the MCCs.

Slow V_p anomalies (< −10%) below the receiver function Moho (Features G, H) have absolute velocities in the range of 6.8 to 7.3 km/s. These anomalies are also observed in the horizontal section from 30 km to 40 km depth along the Hellenic fore-arc (below northern Peloponnese, Fig. 7). The low velocity anomalies appear to follow the Moho of the subducting African plate and probably lie above the top of the subducting slab (Feature H). The low Vp/Vs and high absolute V_p of these anomalies (comparable to silicic metamorphic rocks) suggests that these may have less mafic composition (Brocher, 2005). Halpaap et al. (2018) in their tomography study of the western Hellenic Subduction Zone also observed this low V_p/V_s zone and interpreted it as a silica enrichment zone. They proposed that fluids flowing updip along the sealed interface of the subducting crust leads to silica enrichment that forms the base of the overlying crust. However, this zone does not elongate horizontally, unlike the images of Halpaap et al. (2018) that exhibit an elongation of at least 100 km away from the dipping slab. Another possible source of this anomaly could be the basal underplating of material derived from the subducting crust, which follows the retreating slab like an orogenic wedge (Gallen et al., 2014). This interpretation is supported by the wedge-shaped geometry of this anomaly with limited spatial extent. It is then likely that the underplated materials containing sediments as well as components of upper oceanic crust undergo metamorphism and are assimilated to the base of the Aegean crust, resulting in thickening of the lower crust and a deeper Aegean Moho.

The basal underplating of the Aegean crust is also cited as one of the reasons for the large uplift of paleoshorelines in Crete (Gallen et al., 2014; Strobl et al., 2014). Although it is reasonable that the underplating of the crust may gradually influence topographic relief, such features may not necessarily generate rapid coastline uplift. The data for paleoshoreline uplift indicates that large uplift is restricted to the southern and western shorelines of Crete (Mouslopoulou et al., 2015). We also observe thickened areas of low V_p anomalies and low V_p/V_s in the cross-sections across Crete. However, we do not have enough depth resolution in this part of Aegean to ascertain the exact dimensions of these anomalies.

4.2. Fluid–induced earthquake clusters?

During the visualization process of the tomographic results, it became apparent that several earthquake clusters in well-resolved areas exhibited near-vertical orientation. Such clusters may indicate crack propagation associated with the path of fluid migration from a deeper source to the surface. Fig. 11 shows depth cross-sections of our model along these areas with the earthquake clusters superimposed. As the LOTOS algorithm only provides travel time residuals rather than formal uncertainties, only the events with average residuals <0.20 s for both P and S arrivals as well as having at least four P phases and two S phases

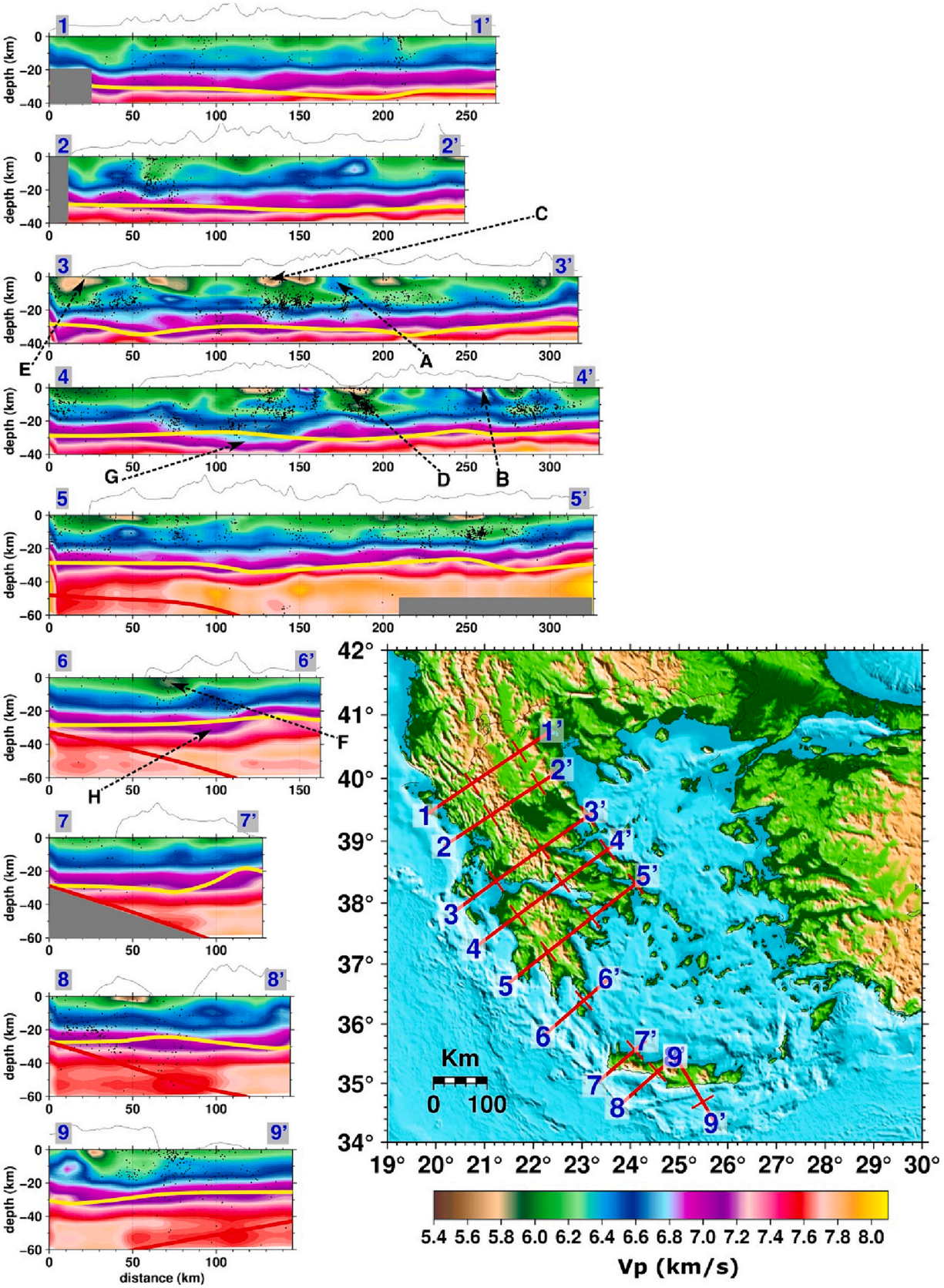

Fig. 10. Absolute V_p anomalies along the Hellenic arc in vertical cross-sections numbered from 1 to 1′ to 9–9′ (same as Fig. 9). Both Aegean Moho (yellow line) and the African Moho (red line) derived from Sodoudi et al. (2006) are outlined. The small black dots in each cross-section indicate relocated earthquakes, within 5 km of its strike. Areas that were not resolved in vertical resolution tests are masked with grey rectangles. Specific anomalies are marked with bold-faced capitalized letters. (For interpretation of the references to colour in this figure legend, the reader is referred to the web version of this article.)

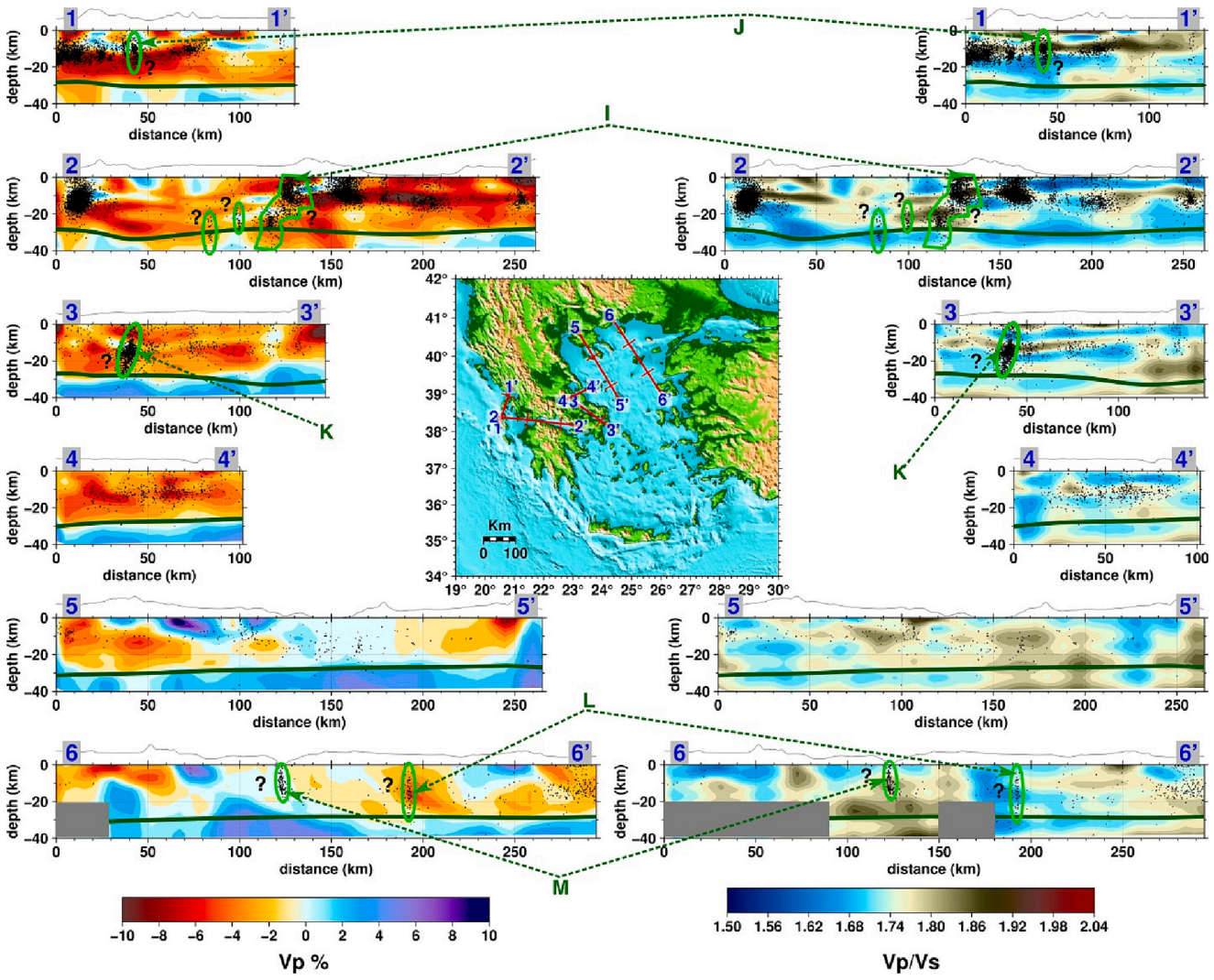

Fig. 11. V_p anomalies and V_p/V_s ratio along the major shear/rift zones in vertical cross-sections: 1–1′ (Kefalonia Transform Zone), 2–2′ (gulf of Corinth), 3–3′ (gulf of Evia), 4–4′ (gulf of Volos and the western termination of North Aegean Trough (NAT)), and 5–5′ and 6–6′ (across NAT). Small black dots in each cross-section indicate relocated earthquakes within 5 km of the cross-section strike after tomographic inversion. The areas that were not well resolved in vertical resolution tests are masked with grey rectangles. Green ellipses mark near-vertical orientation of seismicity likely related to fluids. The Aegean Moho is outlined (dark green line) based on Sodoudi et al. (2006). (For interpretation of the references to colour in this figure legend, the reader is referred to the web version of this article.)

are shown. Considering average values for crustal velocities of 7 ± 0.5 km/s for the P phases and 4 ± 0.5 km/s from the S phases derived from our model, the earthquake location error for the selected events corresponds to about 1.5 km or less. In what follows we present these features with the caveat that relative relocation should be performed in future studies in order to ascertain that the vertical orientation of these clusters is a robust characteristic.

The western Corinth rift has experienced multiple earthquake swarms over the years where the clustered epicenters and high cross-correlation between the earthquake waveforms have been interpreted as the result of fluid activity (Mesimeri and Karakostas, 2018; Mesimeri et al., 2019; Pacchiani and Lyon-Caen, 2010). We observe a continuous zone of earthquake activity in the western Corinth rift, extending from below the crust to the shallow upper crust (Fig. 11: Feature I). The continuity of earthquake activity across high V_p/V_s zones and their clustering near previous locations of earthquake swarms (Duverger et al., 2018) suggests that these may represent migration pathways of fluids from the mantle up to the upper Aegean crust. Other depth cross-sections also show similar near-vertical clusters that have been highlighted with green outlines (Fig. 11: Features J to M), near the Kefalonia Transform zone (Fig. 11: Feature J), the NAT and the gulf of Evia (Fig. 11: Features L and M).

4.3. Active volcanoes and melt fraction

We estimated porosity distribution in the high V_p/V_s (> 1.77) zones beneath the three major volcanic groups using Gassmann's equations (Nur et al., 1991). Gassmann's equations are widely used to estimate porosity in fluid-bearing rocks, assuming a closed system, isotropic constituents, a homogeneous skeleton, and uniform fluid pressure (Sevostianov, 2020). In order to make use of these equations, we have made assumptions on their parameters based on the tectonic/volcanic setting of the Aegean. The formulations of the adopted method as well as the assumed values of the parameters are provided in Text S2 and Table S2. In order to analyze uncertainties in porosity calculation due to errors in the estimation of V_p/V_s, we randomly perturbed the V_p/V_s values in the cross-sections by an upper bound of 3.5%, 7%, and 10%, and performed porosity modeling as shown in Fig. S25. Even with upper bound errors as large as 10%, the porosity estimate is quite close to the original, which shows that they are accurate within reasonable bounds of V_p/V_s estimation error. The results of the porosity distribution are shown in cross-sections along with the V_p/V_s in Fig. 12. At this point it

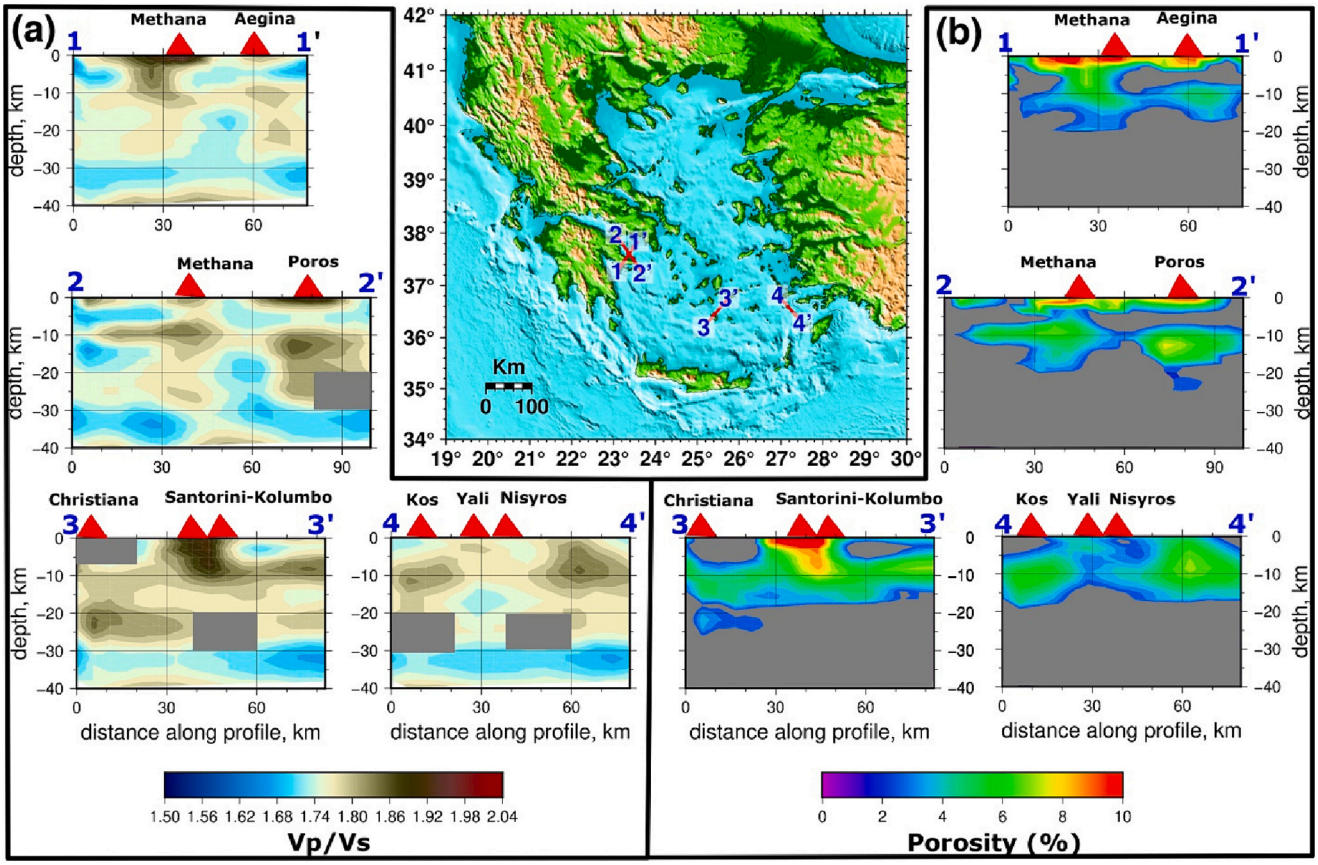

Fig. 12. (a) V_p/V_s ratio below the volcanoes in the SAAVA and (b) estimated porosity using Gassmann's equations. The areas with V_p/V_s <1.77 as well as areas with <1% porosity are masked in (b) with grey colour.

should be noted that porosity does not automatically translate into melt fraction, however, higher porosity crustal rocks may potentially be filled with fluids that are sourced from larger depths.

Cross-sections along Poros-Methana-Aegina, Christiana-Santorini-Kolumbo, and Kos-Yali-Nisyros indicate high V_p/V_s values, which are associated with the magmatic activity beneath these centers. Geochemical studies broadly indicate a three-stage magma differentiation for the SAAVA: a less hydrated, deeper mafic magma source (~ 16+ km), a zone of magma transport and fractionation to silicic composition (8–16 km), and a shallow zone of cystal-mush accumulation (4–8 km) (Andújar et al., 2016; Popa et al., 2019, 2020). Distinct zones of high V_p/V_s in the cross-sections probably indicate differentiated zones of magma below the three major volcanic groups in the Aegean.

Beneath Methana, Aegina, and Poros, high V_p/V_s is observed at three different depth levels: a shallowest (< 3 km) moderately high to high V_p/V_s zone, followed by an intermediate (7–15 km depth) moderately high to high V_p/V_s zone and a deep (15–25 km) moderately high V_p/V_s zone (Fig. 12: 1–1′, 2–2′). Methana-Aegina-Poros group has one of the best station density and azimuthal coverage among the SAAVA volcanoes. As a result, the vertical resolution tests (20 km × 20 km) show the highest depth and lateral resolution (Fig. S17). The porosity modeling using Gassmann's equations indicates up to 10% melt fraction at the shallowest levels (< 3 km), however, at larger depths smaller values (5–8%) are observed. The V_p/V_s zones are well correlated with the three depth levels of magma differentiation. The deeper melting zone is close to the basalt-andesite conversion depth (15–16 km), according to geochemical studies (Popa et al., 2020), and could indicate an accumulation of andesitic melt that serves as the deeper magma reservoir. The continuous zone at 5–15 km depth beneath Methana with 5–8% melt fraction is likely associated with the melt transport pathways to the crystal-mush region (Popa et al., 2020).

A continuous high to very high V_p/V_s zone from the surface down to 15 km depth is observed beneath Santorini-Kolumbo. Even though Santorini has the highest station density among the volcanoes in SAAVA, poor azimuthal coverage implies that good vertical resolution is available only down to 10 km depth. The deeper moderately high to high V_p/V_s zone (10–30 km) beneath Christiana may not be fully resolved (Fig. S17). Porosity modeling indicates around 6–10% melt fraction coinciding with the high V_p/V_s zone beneath Santorini-Kolumbo. These values are within the range estimated by McVey et al. (2020) (2–7% to 3–10%) for a low velocity anomaly extending northeast from the caldera. The large region of high melt fraction suggests higher volume of melting beneath Santorini than Poros-Methana-Aegina, a result supported by geochemical studies (Francalanci and Zellmer, 2019). In relation to the plumbing system beneath Santorini our results have two alternative interpretations: either that magma differentiation occurs in a semi-continuous zone from the surface down to larger depths; or that the continuous zone we imaged, consists of two distinct (shallow and deeper) magma chambers. Unfortunately, the resolution of our model does not allow to distinguish which of these two interpretations is more likely.

Kos-Yali-Nisyros group exhibits a shallow localized moderately high V_p/V_s zone beneath Yali. The vertical resolution test using 20 km anomalies suggest only the top 10 km depth close to the Yali-Nisyros caldera is well resolved. Therefore, the high V_p/V_s zones beneath Kos and to the south of Nisyros are not well resolved, even though moderately high V_p/V_s has been observed in this area in a previous tomography study (Papadimitriou et al., 2018). The porosity modeling of the moderately high V_p/V_s zone beneath Yali shows only 4–5% melt fraction, implying a lower degree of melting below Kos-Yali-Nisyros compared to Santorini, consistent with geochemical analysis (Francalanci and Zellmer, 2019). Geochemical modeling also indicates a

shallow crystal-mush region (4–8 km) (Klaver et al., 2017; Popa et al., 2019), which is likely rejuvenated by small batches of magma from deeper subduction derived melts. The lower resolution at depths >10 km implies that deeper zones of melt differentiation may not be resolvable beneath Kos-Yali-Nisyros with the present model (Fig. S17).

The results of porosity modeling may have a significant impact on the assessment of volcanic hazard along SAAVA and current efforts to monitor active volcanoes in the area. Santorini caldera has so far attracted the attention of the scientific community as well as that of the civil protection agencies for the reason that its future eruption may affect thousands of tourists (if it occurs during summer) as well as the local inhabitants. This is also justified by our results that show a potentially large volume of high porosity rock, likely filled with melt, beneath Santorini. However, our results also show that the mostly forgotten Methana-Aegina-Poros group hosts underneath it a large reservoir of high porosity rocks that may be filled with melt as well. Considering the close proximity (< 50 km) of this area to Athens, the capital of Greece, it can be concluded that any future volcanic hazard assessment and monitoring planning should take these results into account. Furthermore, our porosity estimates can be utilized in volcanological modeling of magma storage and transportation for the active volcanoes along SAAVA.

4.4. Large earthquakes and velocity anomalies

Tomographic images of the source zones of large earthquakes around the world indicate significant velocity anomalies near their hypocenters. Two major patterns are observed: (1) drastic change in the lithology across a boundary (such as a fault) marked by low to high V_p, V_s or Poisson's ratio around the source zone (Hua et al., 2020; Toyokuni et al., 2021); (2) Low-velocity or high Poisson's ratio indicating migration of fluids possibly from a deeper magma source to mantle wedge melting or a crustal source (Kayal et al., 2002; Wang et al., 2018; Zhao et al., 1996). These fluids can generate zones of weakening or fractures, however, their source may not necessarily be magma, instead it may be related to the dehydration of minerals during metamorphism, sedimentary formation brines, magmatic water or CO_2 (Hickman et al., 1995). High CO_2 fluxes have been measured near active volcanic sites close to the Corinth rift (e.g. D'Alessandro et al., 2006) and Helium isotope ratios in spring waters in NW Peloponnese have indicated the presence of mantle derived fluids (Pik and Marty, 2009). Such fluid activity has also been identified previously, in other parts of the Aegean by repeated earthquake swarms (Becker et al., 2006; Mesimeri et al., 2017; Ruscic et al., 2019). These evidences imply that fluid activity may play an important role in the generation of crustal seismicity in the Aegean.

The rupture area of earthquakes with $M_w \geq 6.0$ is large enough such that their source zone structure can be examined using tomographic images with 20–30 km resolution. Scaling relations between fault rupture length and moment magnitude for the eastern Mediterranean region indicate that earthquakes in the range M_w 6.0–6.9 have rupture lengths of 19–33 km, assuming a rectangular fault plane with 2:1 length-width ratio (Konstantinou, 2014).

We identified 10 large earthquakes in the Aegean that are well studied to look for velocity anomalies near their source region. The hypocenters have been adopted from individual studies (listed in the caption of Fig. 13) with errors that are <2 km in both horizontal and vertical directions. It is interesting to note that one of the selected events, the 2008 earthquake (Mw ~6.4) in NW Peloponnese, had been previously identified as occurring in an unfavorably oriented fault and its generation was interpreted as being the result of overpressured fluids acting at its source (see Konstantinou et al., 2011). In order to check if the tomographic resolution is comparable to the fault plane dimensions,

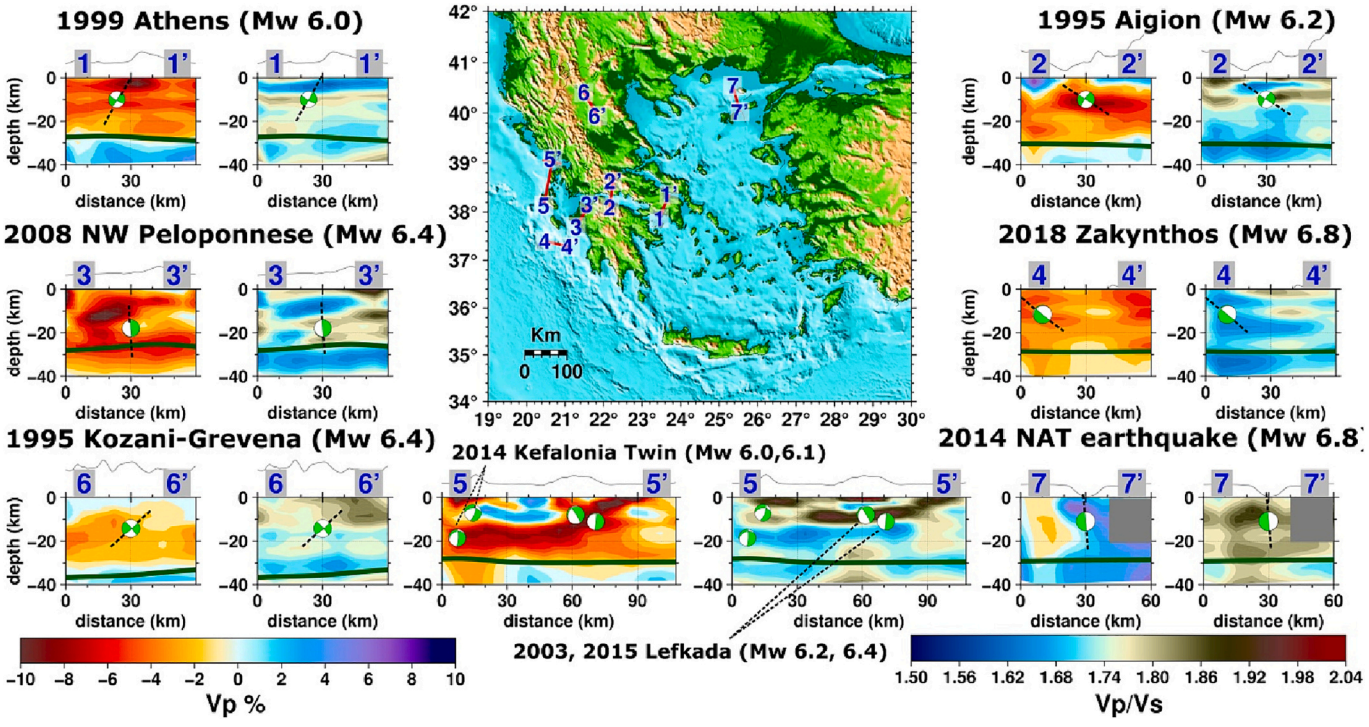

Fig. 13. Cross-sections of P anomalies and V_p/V_s ratios perpendicular to the strikes of selected major crustal earthquakes in the Aegean with their source mechanisms marked using beachballs (green-white) and fault planes shown with black dotted lines. As an exception, cross-section 5–5′ is oriented along KTZ to include multiple earthquakes with near-parallel strikes. The source parameters of these earthquakes are derived from following studies: Bernard et al. (1997) (1995 Aigion earthquake, Mw: 6.2), Papadimitriou et al. (2002) (1999 Athens earthquake, Mw: 6.0), Cirella et al. (2020) (2018 Zakynthos earthquake, Mw: 6.8), Konstantinou et al. (2011) (2008 NW Peloponnese earthquake, Mw: 6.4), Karakostas et al. (2015) (2014, Kefalonia Twin earthquakes, Mw: 6.1, 6.0), Benetatos et al. (2005) & Sokos et al. (2016) (2003 & 2015 Lefkada earthquakes, Mw: 6.2, 6.4), Hatzfeld et al. (1997) (1995 Kozani-Grevena earthquake, Mw: 6.4) and Saltogianni et al. (2015) (2014 NAT earthquake, Mw: 6.8). (For interpretation of the references to colour in this figure legend, the reader is referred to the web version of this article.)

we performed vertical resolution tests with checkerboard grids of 20 km × 20 km × 20 km for M_w 6.0–6.9 earthquakes (Figs. S18, S19, and S20). We present the cross-sections perpendicular to the strike of major earthquakes, whose source zones are well resolved (Fig. 13). Cross-sections parallel to the strike of their focal mechanisms are provided in the supporting information along with the checkerboard test results (Figs. S19, S26). Both strike-parallel and strike-perpendicular cross-sections show similar anomalies in the source zone of these earthquakes.

The selected earthquakes occurred in the well-studied rift/shear zones (the KTZ, the gulf of Corinth and the NAT) as well as along the lesser known fault zones in the western fore-arc, the NW Peloponnese, and mainland Greece. The 2018 Zakynthos earthquake displays thrust-faulting mechanism related to the subduction along the western fore-arc (Cirella et al., 2020). The hypocentral depths of all other earthquakes lie in the upper to middle crustal range (< 20 km) and mainly exhibit normal/strike-slip faulting, which agrees with the extensional stress regime in the Aegean crust (Konstantinou et al., 2017). Most of the earthquake hypocenters are either situated at the boundary between a low V_p zone marked by −2 to −8% anomaly and a high V_p zone marked by +2 to +6% anomaly or exist at the edge of high V_p/V_s (1.8–1.98) zones. The contrasting V_p anomalies near the source zones of these earthquakes imply that they occurred at the interface of lithologies having different composition or strength. The high V_p/V_s suggests that fluid movement along the lithology boundaries may have created weakened zones that were easily ruptured when subjected to small stress increments.

In the case of the 2014 twin Kefalonia earthquakes (Karakostas et al., 2015) and the two Lefkada earthquakes (2003 and 2015) (Benetatos et al., 2005; Sokos et al., 2016), the initial event occurred at a larger depth (> 10 km) in a low V_p zone, while the second event occurred at a high-low V_p contrast. In the context of our results, it seems likely that the second event is a continuation of the rupture propagation of the first one along a fault that had been weakened by fluids. The first Kefalonia event occurred above a moderately high V_p/V_s zone, however, the very low V_p (−6 to −8%) in the source zone suggests a weakened structure. The 2018 Zakynthos earthquake (Cirella et al., 2020) is another special case where no significant contrast in V_p anomaly is observed at the source zone and the V_p/V_s value is very close to the average (1.77). Detailed analysis of its low angle strike-slip faulting mechanism suggests two possible mechanisms, either that it occurred on the subduction interface or that it reactivated an older east-dipping thrust fault (Papadimitriou et al., 2021). It is possible that a very local change in stress brought by a transient fluid pressure increase that generated the earthquake had waned after the rupture.

Some of the other large earthquakes in the Aegean are the 2017 Lesvos earthquake (Kiratzi, 2018), the 2001 Skyros earthquake (Benetatos et al., 2002), the 2017 Bodrum-Kos earthquake (Andinisari et al., 2020), and the 2020 Samos earthquake. The results for these earthquakes are shown in Fig. S27 for the sake of completeness, however, the resolution along the fault plane is limited (Fig. S20) thus prohibiting any definite interpretation of their anomalies.

The correlation of large earthquakes in the Aegean with the velocity anomalies at their source has important implications in terms of seismic hazard in the region and possibly beyond. This correlation puts forward the possibility that fluids may cause the rupture of even unfavorably oriented faults with respect to the present-day stress field (e.g., Konstantinou et al., 2011). In this respect, the tomographic results presented here can be combined with field observations from structural geology, palaeseismology, and geophysical prospecting in order to identify faults that lie near high V_p contrast or high V_p/V_s zones. The same assessment could also be performed for faults that are very near densely populated areas, and/or are overdue to produce large earthquakes (e.g., the Atalanti fault in central Greece). Finally, a significant contribution of these results could be their usage for constraining models of how fluids influence earthquake rupture in extensional tectonic environments similar to the Aegean.

5. Conclusions

We performed body-wave travel time tomography of the Aegean crust using 178,676 events recorded across 324 seismic stations from both permanent and temporary seismic networks in the area. We employed the well-known tomographic inversion software LOTOS-12 (Koulakov, 2009) for both 1-D velocity model optimization and final 3D model generation. The 3D model thus provides velocity structure of the Aegean crust with a high lateral resolution (30 km × 30 km). The tomographic results provide detailed information about the Aegean crustal structure, help assess the degree of melting beneath the active volcanoes and enhance our knowledge of the source mechanisms of large earthquakes. The main conclusions are as follows:

1. The Aegean Moho from receiver function analysis is well correlated with a drastic change in V_p anomaly sign at depths >20 km. Large V_p contrast from low to high velocities at >20 km depths marks the start of the Aegean crust-mantle transition.
2. The slow V_p anomaly in the fore-arc close to the receiver function Moho indicates assimilation of metamorphosed oceanic material to the base of the Aegean crust along the Hellenic arc. The fast V_p anomalies along with high V_p/V_s at upper crustal depths are mafic metamorphosed rocks, which may evolve in a similar manner as metamorphic core complexes.
3. Near-vertical alignment of the relocated earthquake clusters across high V_p/V_s areas along the rift/shear zones suggest that these may represent pathways of fluid migration from the mantle to the upper crust. Further seismological studies are needed in order to definitely confirm this preliminary interpretation.
4. Porosity modeling using tomographic results indicates 4–10% melt fraction on average beneath SAAVA. Although results suggest that the largest volume of melt can be found beneath Santorini, they also reveal large melt fraction values beneath Methana-Aegina-Poros, an observation that should be taken into account in future volcanic hazard assessments and volcano monitoring plans.
5. Source regions of large earthquakes ($M_w \geq 6.0$) display high V_p/V_s and low-high V_p contrast, which suggests that the weakening of the source zone lithologies by fluid migration combined with steadily increasing tectonic stress was the main cause of these earthquake ruptures. Thus, our tomographic model when combined with observations from structural geology, paleoseismology, and geophysical prospecting, can help identify faults near such velocity anomalies and significantly enhance seismic hazard assessment in the Aegean region.

CRediT authorship contribution statement

P. Ranjan: Writing – review & editing, Writing – original draft, Visualization, Validation, Methodology, Investigation, Formal analysis. **K.I. Konstantinou:** Writing – review & editing, Validation, Supervision, Resources, Project administration, Funding acquisition, Conceptualization.

Declaration of competing interest

The authors declare that they have no known competing financial interests or personal relationships that could have appeared to influence the work reported in this paper.

Data availability

The EGELADOS and CYCNET waveform data are freely available for download from GFZ, Potsdam, European Integrated Data Archive (EIDA) (http://eida.gfz-potsdam.de/webdc3/) under the network code Z3 and ZZ. The phase picks for the HUSN data are freely available for download from the National Observatory of Athens (NOA) website

(http://gein.noa.gr/). The station listing used in the phase files were obtained from the European Integrated Data Archive (EIDA) web portal at NOA (http://eida.gein.noa.gr/webdc3/). The LOTOS code is freely available for download from http://www.ivan-art.com/science/LOTOS/. All the figures were generated using Generic Mapping Tools (GMT), version 6 (Wessel et al., 2019) and compiled with Inkscape software (https://inkscape.org/). For tomography related figures, a perl (https://www.perl.org/) script was used for parsing files to GMT. All the scripts for generating figures and the travel times/station data files used in this work are accessible via zenodo.org at https://zenodo.org/records/11070245.

Acknowledgments

We thank Kori Fajar Hermawan for picking phase arrivals and locating initial hypocenters for part of the CYCNET data. We also thank Ratri Andinisari for useful discussions during the analysis phase of this work. This research was funded by Taiwan International Graduate Program (TIGP) scholarship (P. Ranjan) and Ministry of Science and Technology (MOST), Taiwan grant 110-2116-M-008-016 (K. I. Konstantinou). We are also grateful to Dr. Prakash Kumar (Director, CSIR-National Geophysical Research Institute, India) for providing computational facilities that helped in revising parts of the manuscript.

Appendix A. Supplementary data

Supplementary data to this article can be found online at https://doi.org/10.1016/j.tecto.2024.230331.

References

Amante, C., Eakins, B.W., 2009. ETOPO1 1 arc-minute global relief model: Procedures, data sources and analysis. In: NOAA Technical Memorandum NESDIS NGDC-24, vol. 10. National Geophysical Data Center, NOAA, p. V5C8276M. doi: 10.7289/V5C8276M.

Andinisari, R., Konstantinou, K.I., Ranjan, P., 2020. Seismotectonics of SE Aegean inferred from precise relative locations of shallow crustal earthquakes. J. Seismol. 24, 1–22. https://doi.org/10.1007/s10950-019-09881-8.

Andújar, J., Scaillet, B., Pichavant, M., Druitt, T.H., 2016. Generation Conditions of Dacite and Rhyodacite via the Crystallization of an Andesitic Magma. Implications for the Plumbing System at Santorini (Greece) and the Origin of Tholeiitic or Calc-alkaline Differentiation Trends in Arc Magmas. J. Petrol. 57 (10), 1887–1920. https://doi.org/10.1093/petrology/egw061.

Aristotle University Of Thessaloniki Seismological Network, 1981. Permanent Regional Seismological Network operated by the Aristotle University of Thessaloniki. International Federation of Digital Seismograph Networks. https://doi.org/10.7914/SN/HT.

Becker, D., Meier, T., Rische, M., Bohnhoff, M., Harjes, H.P., 2006. Spatio-temporal microseismicity clustering in the Cretan region. Tectonophysics 423 (1–4), 3–16. https://doi.org/10.1016/j.tecto.2006.03.022.

Benetatos, C., Roumelioti, Z., Kiratzi, A., Melis, N., 2002. Source parameters of the M 6.5 skyros Island (North Aegean Sea) earthquake of July 26, 2001. Ann. Geophys. 45 (3–4), 513–526. https://doi.org/10.4401/ag-3525.

Benetatos, C., Kiratzi, A., Roumelioti, Z., Stavrakakis, G., Drakatos, G., Latoussakis, I., 2005. The 14 August 2003 Lefkada Island (Greece) earthquake: Focal mechanisms of the mainshock and of the aftershock sequence. J. Seismol. 9 (2), 171–190. https://doi.org/10.1007/s10950-005-7092-1.

Bernard, P., Briole, P., Meyer, B., Lyon-Caen, H., Gomez, J.-M., Tiberi, C., et al., 1997. The Ms = 6.2, June 15, 1995 Aigion earthquake (Greece): evidence for low angle normal faulting in the Corinth rift. J. Seismol. 1 (2), 131–150. https://doi.org/10.1023/A:1009795618839.

Bijwaard, H., Spakman, W., Engdahl, E.R., 1998. Closing the gap between regional and global travel time tomography. J. Geophys. Res. Solid Earth 103 (B12), 30055–30078. https://doi.org/10.1029/98JB02467.

Blom, N., Gokhberg, A., Fichtner, A., 2020. Seismic waveform tomography of the central and eastern Mediterranean upper mantle. Solid Earth 11 (2), 669–690. https://doi.org/10.5194/se-11-669-2020.

Bocchini, G.M., Brüstle, A., Becker, D., Meier, T., van Keken, P.E., Ruscic, M., et al., 2018. Tearing, segmentation, and backstepping of subduction in the Aegean: New insights from seismicity. Tectonophysics 734–735, 96–118. https://doi.org/10.1016/j.tecto.2018.04.002.

Bondár, I., Myers, S.C., Engdahl, E.R., Bergman, E.A., 2004. Epicentre accuracy based on seismic network criteria. Geophys. J. Int. 156, 483–496. https://doi.org/10.1111/j.1365-246X.2004.02070.x.

Boschi, E., Giardini, D., Morelli, A., 1991. MedNet: the very broad-band seismic network for the Mediterranean. Il Nuovo Cimento C 14 (1), 79–99. https://doi.org/10.1007/BF02509260.

Brocher, T.M., 2005. Empirical relations between elastic wavespeeds and density in the Earth's crust. Bull. Seismol. Soc. Am. 95 (6), 2081–2092. https://doi.org/10.1785/0120050077.

Brüstle, A., 2013. Seismicity of the eastern Hellenic Subduction Zone. Retrieved from. https://hss-opus.ub.ruhr-uni-bochum.de/opus4/frontdoor/index/index/docId/1127.

Burchfiel, B.C., Royden, L.H., Papanikolaou, D., Pearce, F.D., 2018. Crustal development within a retreating subduction system: the Hellenides. Geosphere 14 (3), 1119–1130. https://doi.org/10.1130/GES01573.1.

Cambaz, M.D., Turhan, F., Yılmazer, M., Kekovalı, K., Necmioğlu, Ö., Kalafat, D., 2019. A review on Kandilli Observatory and Earthquake Research Institute (KOERI) seismic network and earthquake catalog: 2008–2018. Adv. Geosci. 51, 15–23. https://doi.org/10.5194/adgeo-51-15-2019.

Caputo, R., Chatzipetros, A., Pavlides, S., Sboras, S., 2013. The Greek Database of Seismogenic sources (GreDaSS): state-of-the-art for northern Greece. Ann. Geophys. 55 (5) https://doi.org/10.4401/ag-5168.

Carbonell, R., Levander, A., Kind, R., 2013. The Mohorovičić discontinuity beneath the continental crust: an overview of seismic constraints. Tectonophysics. https://doi.org/10.1016/j.tecto.2013.08.037. Elsevier B.V.

Christensen, N.I., 1996. Poisson's ratio and crustal seismology. J. Geophys. Res. Solid Earth 101 (B2), 3139–3156. https://doi.org/10.1029/95JB03446.

Christensen, N.I., Mooney, W.D., 1995. Seismic velocity structure and composition of the continental crust: a global view. J. Geophys. Res. Solid Earth 100 (B6), 9761–9788. https://doi.org/10.1029/95JB00259.

Cirella, A., Romano, F., Avallone, A., Piatanesi, A., Briole, P., Ganas, A., et al., 2020. The 2018 Mw 6.8 Zakynthos (Ionian Sea, Greece) earthquake: seismic source and local tsunami characterization. Geophys. J. Int. 221 (2), 1043–1054. https://doi.org/10.1093/gji/ggaa053.

Corinth Rift Laboratory Team And RESIF Datacenter, 2013. CL - Corinth Rift Laboratory Seismological Network (CRLNET) [Data set]. RESIF - Réseau Sismologique et géodésique Français. https://doi.org/10.15778/RESIF.CL.

D'Alessandro, W., Brusca, L., Kyriakopoulos, K., Rotolo, S., Michas, G., Minio, M., Papadakis, G., 2006. Diffuse and focused carbon dioxide and methane emissions from the Sousaki geothermal system, Greece. Geophys. Res. Lett. 33 (5), L05307. https://doi.org/10.1029/2006GL025777.

D'Alessandro, A., Papanastassiou, D., Baskoutas, I., 2011. Hellenic Unified Seismological Network: an evaluation of its performance through SNES method. Geophys. J. Int. 185 (3), 1417–1430. https://doi.org/10.1111/j.1365-246X.2011.05018.x.

Dimitriadis, I., Papazachos, C., Panagiotopoulos, D., Hatzidimitriou, P., Bohnhoff, M., Rische, M., Meier, T., 2010. P and S velocity structures of the Santorini-Coloumbo volcanic system (Aegean Sea, Greece) obtained by non-linear inversion of travel times and its tectonic implications. J. Volcanol. Geotherm. Res. 195 (1), 13–30. https://doi.org/10.1016/j.jvolgeores.2010.05.013.

Duverger, C., Lambotte, S., Bernard, P., Lyon-Caen, H., Deschamps, A., Nercessian, A., 2018. Dynamics of microseismicity and its relationship with the active structures in the western Corinth Rift (Greece). Geophys. J. Int. 215 (1), 196–221. https://doi.org/10.1093/gji/ggy264.

Endrun, B., Meier, T., Lebedev, S., Bohnhoff, M., Stavrakakis, G., Harjes, H.P., 2008. S velocity structure and radial anisotropy in the Aegean region from surface wave dispersion. Geophys. J. Int. 174 (2), 593–616. https://doi.org/10.1111/j.1365-246X.2008.03802.x.

Floyd, M.A., et al., 2010. A new velocity field for Greece: Implications for the kinematics and dynamics of the Aegean. J. Geophys. Res. 115, B10403. https://doi.org/10.1029/2009JB007040.

Francalanci, L., Zellmer, G.F., 2019. Magma genesis at the South Aegean volcanic arc. Elements 15 (3), 165–170. https://doi.org/10.2138/gselements.15.3.165.

Friederich, W., Meier, T., 2008. Temporary seismic broadband network acquired data on Hellenic Subduction Zone. EOS Trans. Am. Geophys. Union 89 (40), 378. https://doi.org/10.1029/2008EO400002.

Fukao, Y., Widiyantoro, S., Obayashi, M., 2001. Stagnant slabs in the upper and lower mantle transition region. Rev. Geophys. 39 (3), 291–323. https://doi.org/10.1029/1999RG000068.

Fytikas, M., Vougioukalakis, G., 2005. The South Aegean Active Volcanic Arc: Present Knowledge and Future Perspectives. Elsevier. https://doi.org/10.1007/s00445-011-0529-1.

Gallen, S.F., Wegmann, K.W., Bohnenstiehl, D.R., Pazzaglia, F.J., Brandon, M.T., Fassoulas, C., 2014. Active simultaneous uplift and margin-normal extension in a forearc high, Crete, Greece. Earth Planet. Sci. Lett. 398, 11–24. https://doi.org/10.1016/j.epsl.2014.04.038.

García, M.A., Vargas, C.A., Koulakov, I.Y., 2019. Local earthquake tomography of the Nevado del Huila Volcanic complex (Colombia): magmatic and tectonic interactions in a Volcanic-Glacier Complex System. J. Geophys. Res. Solid Earth 124 (2), 1688–1699. https://doi.org/10.1029/2018JB016324.

Gesret, A., Laigle, M., Diaz, J., Sachpazi, M., Charalampakis, M., Hirn, A., 2011. Slab top dips resolved by teleseismic converted waves in the Hellenic subduction zone. Geophys. Res. Lett. 38 (20), n/a–n/a. https://doi.org/10.1029/2011GL048996.

Govers, R., Fichtner, A., 2016. Signature of slab fragmentation beneath Anatolia from full-waveform tomography. Earth Planet. Sci. Lett. 450, 10–19. https://doi.org/10.1016/j.epsl.2016.06.014.

Halpaap, F., Rondenay, S., Ottemöller, L., 2018. Seismicity, deformation, and metamorphism in the Western Hellenic Subduction Zone: new constraints from tomography. J. Geophys. Res. Solid Earth 123 (4), 3000–3026. https://doi.org/10.1002/2017JB015154.

Hansen, S.E., Evangelidis, C.P., Papadopoulos, G.A., 2019. Imaging slab detachment within the Western Hellenic Subduction Zone. Geochem. Geophys. Geosyst. 20 (2), 895–912. https://doi.org/10.1029/2018GC007810.

Hatzfeld, D., Karakostas, V., Ziazia, M., Selvaggi, G., Leborgne, S., Berge, C., et al., 1997. The Kozani-Grevena (Greece) earthquake of 13 May 1995 revisited from a detailed seismological study. Bull. Seismol. Soc. Am. 87 (2), 463–473. https://doi.org/10.1785/gssrl.66.6.61.

Heath, B.A., Hooft, E.E.E., Toomey, D.R., Papazachos, C.B., Nomikou, P., Paulatto, M., et al., 2019. Tectonism and its relation to magmatism around Santorini Volcano from Upper Crustal P Wave Velocity. J. Geophys. Res. Solid Earth 124 (10), 10610–10629. https://doi.org/10.1029/2019JB017699.

Hickman, S., Sibson, R., Bruhn, R., 1995. Introduction to special section: mechanical involvement of fluids in faulting. J. Geophys. Res. Solid Earth 100 (B7), 12831–12840. https://doi.org/10.1029/95jb01121.

Hooft, E.E.E., Heath, B.A., Toomey, D.R., Paulatto, M., Papazachos, C.B., Nomikou, P., et al., 2019. Seismic imaging of Santorini: Subsurface constraints on caldera collapse and present-day magma recharge. Earth Planet. Sci. Lett. 514, 48–61. https://doi.org/10.1016/j.epsl.2019.02.033.

Hua, Y., Zhao, D., Toyokuni, G., Xu, Y., 2020. Tomography of the source zone of the great 2011 Tohoku earthquake. Nat. Commun. 11 (1), 1163. https://doi.org/10.1038/s41467-020-14745-8.

Huet, B., Le Pourhiet, L., Labrousse, L., Burov, E., Jolivet, L., 2011. Post-orogenic extension and metamorphic core complexes in a heterogeneous crust: the role of crustal layering inherited from collision. Application to the Cyclades (Aegean domain). Geophys. J. Int. 184 (2), 611–625. https://doi.org/10.1111/j.1365-246X.2010.04849.x.

Institute of Engineering Seimology Earthquake Engineering (ITSAK), 1981. ITSAK Strong Motion Network. International Federation of Digital Seismograph Networks. https://doi.org/10.7914/SN/HI.

Johnston, J.E., Christensen, N.I., 1992. Shear wave reflectivity, anisotropies, Poisson's ratios, and densities of a southern Appalachian Paleozoic sedimentary sequence. Tectonophysics 210 (1–2), 1–20. https://doi.org/10.1016/0040-1951(92)90124-O.

Jolivet, L., Brun, J.P., 2010. Cenozoic geodynamic evolution of the Aegean. Int. J. Earth Sci. 99 (1), 109–138. https://doi.org/10.1007/s00531-008-0366-4.

Jolivet, L., Faccenna, C., Huet, B., Labrousse, L., Le Pourhiet, L., Lacombe, O., et al., 2013. Aegean tectonics: Strain localisation, slab tearing and trench retreat. Tectonophysics. https://doi.org/10.1016/j.tecto.2012.06.011. Elsevier B.V.

Kapetanidis, V., Kassaras, I., 2019. Contemporary crustal stress of the Greek region deduced from earthquake focal mechanisms. J. Geodyn. 123, 55–82. https://doi.org/10.1016/j.jog.2018.11.004.

Karagianni, E.E., Papazachos, C.B., Panagiotopoulos, D.G., Suhadolc, P., Vuan, A., Panza, G.F., 2005. Shear velocity structure in the Aegean area obtained by inversion of Rayleigh waves. Geophys. J. Int. 160 (1), 127–143. https://doi.org/10.1111/j.1365-246X.2005.02354.x.

Karakonstantis, A., Papadimitriou, P., Millas, C., Spingos, I., Fountoulakis, I., Kaviris, G., 2019. Tomographic imaging of the NW edge of the Hellenic volcanic arc. J. Seismol. 23 (5), 995–1016. https://doi.org/10.1007/s10950-019-09849-8.

Karakostas, V., Papadimitriou, E., Mesimeri, M., Gkarlaouni, C., Paradisopoulou, P., 2015. The 2014 Kefalonia Doublet (Mw 6.1 and Mw 6.0), Central Ionian Islands, Greece: Seismotectonic implications along the Kefalonia transform fault zone. Acta Geophys. 63 (1), 1–16. https://doi.org/10.2478/s11600-014-0227-4.

Kassaras, I., Kapetanidis, V., Karakonstantis, A., Papadimitriou, P., 2020. Deep structure of the Hellenic lithosphere from teleseismic Rayleigh-wave tomography. Geophys. J. Int. 221 (1), 205–230. https://doi.org/10.1093/gji/ggz579.

Kayal, J.R., Zhao, D., Mishra, O.P., De, R., Singh, O.P., 2002. The 2001 Bhuj earthquake: Tomographic evidence for fluids at the hypocenter and its implications for rupture nucleation. Geophys. Res. Lett. 29 (24) https://doi.org/10.1029/2002GL015177, 5-1-5-4.

Kiratzi, A., 2018. The 12 June 2017 Mw 6.3 Lesvos Island (Aegean Sea) earthquake: Slip model and directivity estimated with finite-fault inversion. Tectonophysics 724–725, 1–10. https://doi.org/10.1016/j.tecto.2018.01.003.

Klaver, M., Matveev, S., Berndt, J., Lissenberg, C.J., Vroon, P.Z., 2017. A mineral and cumulate perspective to magma differentiation at Nisyros volcano, Aegean arc. Contrib. Mineral. Petrol. 172 (11−12), 95. https://doi.org/10.1007/s00410-017-1414-5.

Konstantinou, K.I., 2014. Moment magnitude–rupture area scaling and stress-drop variations for Earthquakes in the Mediterranean region. Bull. Seismol. Soc. Am. 104 (5), 2378–2386. https://doi.org/10.1785/0120140062.

Konstantinou, K.I., 2020. Magma chamber evolution during the 1650 AD Kolumbo eruption provides clues about past and future volcanic activity. Sci. Rep. 10 (1), 1–12. https://doi.org/10.1038/s41598-020-71991-y.

Konstantinou, K.I., Evangelidis, C.P., Melis, N.S., 2011. The 8 June 2008 M w 6.4 earthquake in Northwest Peloponnese, Western Greece: a Case of Fault Reactivation in an Overpressured lower Crust? Bull. Seismol. Soc. Am. 101 (1), 438–445. https://doi.org/10.1785/0120100074.

Konstantinou, K.I., Mouslopoulou, V., Liang, W.-T., Heidbach, O., Oncken, O., Suppe, J., 2017. Present-day crustal stress field in Greece inferred from regional-scale damped inversion of earthquake focal mechanisms. J. Geophys. Res. Solid Earth 122 (1), 506–523. https://doi.org/10.1002/2016JB013272.

Konstantinou, K.I., Syahra, V., Ranjan, P., 2021. Crustal anisotropy in the southern Aegean from shear wave splitting of local earthquakes. J. Geodyn. 143, 101810 https://doi.org/10.1016/j.jog.2020.101810.

Koulakov, I., 2009. LOTOS Code for local Earthquake Tomographic Inversion: Benchmarks for Testing Tomographic Algorithms. Bull. Seismol. Soc. Am. 99 (1), 194–214. https://doi.org/10.1785/0120080013.

Koulakov, I., Komzeleva, V., Abkadyrov, I., Kugaenko, Y., El Khrepy, S., Al Arifi, N., 2019. Unrest of the Udina volcano in Kamchatka inferred from the analysis of seismicity and seismic tomography. J. Volcanol. Geotherm. Res. 379, 45–59. https://doi.org/10.1016/j.jvolgeores.2019.05.006.

Lallemand, S., Heuret, A., Boutelier, D., 2005. On the relationships between slab dip, back-arc stress, upper plate absolute motion, and crustal nature in subduction zones. Geochem. Geophys. Geosyst. 6 (9) https://doi.org/10.1029/2005GC000917 n/a-n/a.

Lambotte, S., Lyon-Caen, H., Bernard, P., Deschamps, A., Patau, G., Nercessian, A., et al., 2014. Reassessment of the rifting process in the Western Corinth Rift from relocated seismicity. Geophys. J. Int. 197 (3), 1822–1844. https://doi.org/10.1093/gji/ggu096.

Latorre, D., Virieux, J., Monfret, T., Monteiller, V., Vanorio, T., Got, J.L., Lyon-Caen, H., 2004. A new seismic tomography of Aigion area (Gulf of Corinth, Greece) from the 1991 data set. Geophys. J. Int. 159 (3), 1013–1031. https://doi.org/10.1111/j.1365-246X.2004.02412.x.

Li, X., Bock, G., Vafidis, A., Kind, R., Harjes, H.P., Hanka, W., et al., 2003. Receiver function study of the Hellenic subduction zone: Imaging crustal thickness variations and the oceanic Moho of the descending African lithosphere. Geophys. J. Int. 155 (2), 733–748. https://doi.org/10.1046/j.1365-246X.2003.02100.x.

Lomax, A., Virieux, J., Volant, P., Berge-Thierry, C., 2000. Probabilistic Earthquake Location in 3D and Layered Models. Springer, Dordrecht, pp. 101–134. https://doi.org/10.1007/978-94-015-9536-0_5.

McVey, B.G., Hooft, E.E.E., Heath, B.A., Toomey, D.R., Paulatto, M., Morgan, J.V., et al., 2020. Magma accumulation beneath Santorini volcano, Greece, from P-wave tomography. Geology 48 (3), 231–235. https://doi.org/10.1130/G47127.1.

Meier, T., Bohnhoff, M., Harjes, H.-P., 2004. Cyclades Project 2002–2005 and Libyan Sea Offshore Project 2003–2004, RUB Bochum, Germany. Deutsches GeoForschungsZentrum GFZ. https://doi.org/10.14470/MM7557265463.

Mesimeri, M., Karakostas, V., 2018. Repeating earthquakes in western Corinth Gulf (Greece): implications for aseismic slip near locked faults. Geophys. J. Int. 215 (1), 659–676. https://doi.org/10.1093/gji/ggy301.

Mesimeri, M., Karakostas, V., Papadimitriou, E., Tsaklidis, G., Tsapanos, T., 2017. Detailed microseismicity study in the area of Florina (Greece): evidence for fluid driven seismicity. Tectonophysics 694, 424–435. https://doi.org/10.1016/j.tecto.2016.11.027.

Mesimeri, M., Karakostas, V., Papadimitriou, E., Tsaklidis, G., 2019. Characteristics of earthquake clusters: Application to western Corinth Gulf (Greece). Tectonophysics 767, 228160. https://doi.org/10.1016/j.tecto.2019.228160.

Mouslopoulou, V., Nicol, A., Begg, J., Oncken, O., Moreno, M., 2015. Clusters of megaearthquakes on upper plate faults control the Eastern Mediterranean hazard. Geophys. Res. Lett. 42 (23), 10282–10289. https://doi.org/10.1002/2015GL066371.

National Observatory of Athens, I.O.G., 1997. National Observatory of Athens Seismic Network. International Federation of Digital Seismograph Networks. https://doi.org/10.7914/SN/HL.

Nur, A., Marion, D., Yin, H., 1991. In: Hovem, J.M., Richardson, M.D., Stoll, R.D. (Eds.), Wave Velocities in Sediments BT - Shear Waves in Marine Sediments. Springer Netherlands, Dordrecht, pp. 131–140. https://doi.org/10.1007/978-94-011-3568-9_15.

Özbakir, A.D., Govers, R., Fichtner, A., 2020. The Kefalonia Transform Fault: a STEP fault in the making. Tectonophysics 787, 228471. https://doi.org/10.1016/j.tecto.2020.228471.

Pacchiani, F., Lyon-Caen, H., 2010. Geometry and spatio-temporal evolution of the 2001 Agios Ioanis earthquake swarm (Corinth Rift, Greece). Geophys. J. Int. 180 (1), 59–72. https://doi.org/10.1111/j.1365-246X.2009.04409.x.

Paige, C.C., Saunders, M.A., 1982. LSQR: an algorithm for sparse linear equations and sparse least squares. ACM Trans. Math. Softw. (TOMS) 8 (1), 43–71. https://doi.org/10.1145/355984.355989.

Papadimitriou, P., Voulgaris, N., Kassaras, I., Kaviris, G., Delibasis, N., Makropoulos, K., 2002. The Mw = 6.0, 7 September 1999 Athens Earthquake. Nat. Hazards 27 (1), 15–33. https://doi.org/10.1023/A:1019914915693.

Papadimitriou, P., Karakonstantis, A., Kapetanidis, V., Bozionelos, G., Kaviris, G., Voulgaris, N., 2018. In: Dietrich, V.J., Lagios, E. (Eds.), Seismicity and Tomographic Imaging of the Broader Nisyros Region (Greece) BT - Nisyros Volcano: The Kos - Yali - Nisyros Volcanic Field. Springer International Publishing, Cham, pp. 245–271. https://doi.org/10.1007/978-3-319-55460-0_8.

Papadimitriou, P., Kapetanidis, V., Karakonstantis, A., Spingos, I., Pavlou, K., Kaviris, G., et al., 2021. The 25 October 2018 Zakynthos (Greece) earthquake: seismic activity at the transition between a transform fault and a subduction zone. Geophys. J. Int. 225 (1), 15–36. https://doi.org/10.1093/gji/ggaa575.

Papazachos, C., Nolet, G., 1997. P and S deep velocity structure of the Hellenic area obtained by robust nonlinear inversion of travel times. J. Geophys. Res. Solid Earth 102 (B4), 8349–8367. https://doi.org/10.1029/96jb03730.

Papazachos, B.C., Karakostas, V.G., Papazachos, C.B., Scordilis, E.M., 2000. The geometry of the Wadati-Benioff zone and lithospheric kinematics in the Hellenic arc. Tectonophysics 319 (4), 275–300. https://doi.org/10.1016/S0040-1951(99)00299-1.

Pearce, D., Rondenay, S., Sachpazi, M., Charalampakis, M., Royden, L.H., 2012. Seismic investigation of the transition from continental to oceanic subduction along the western Hellenic subduction Zone. J. Geophys. Res. Solid Earth 117 (7). https://doi.org/10.1029/2011JB009023.

Pik, R., Marty, B., 2009. Helium isotopic signature of modern and fossil fluids associated with the Corinth rift fault zone (Greece): Implication for fault connectivity in the lower crust. Chem. Geol. 266 (1–2), 67–75. https://doi.org/10.1016/j.chemgeo.2008.09.024.

Piromallo, C., Morelli, A., 2003. P wave tomography of the mantle under the Alpine-Mediterranean area. J. Geophys. Res. Solid Earth 108 (B2), 2065. https://doi.org/10.1029/2002JB001757.

Pitilakis, K., Roumelioti, Z., Raptakis, D., Manakou, M., Liakakis, K., Anastasiadis, A., Pitilakis, D., 2013. The EUROSEISTEST Strong-Motion Database and Web Portal. Seismol. Res. Lett. 84 (5), 796–804. https://doi.org/10.1785/0220130030.

Podvin, P., Lecomte, I., April 1991. Finite difference computation of trravel times in very contrasted velocity models: a massively parallel approach and its associated tools. Geophys. J. Int. 105 (1), 271–284. https://doi.org/10.1111/j.1365-246X.1991.tb03461.x.

Popa, R.G., Bachmann, O., Ellis, B.S., Degruyter, W., Tollan, P., Kyriakopoulos, K., 2019. A connection between magma chamber processes and eruptive styles revealed at Nisyros-Yali volcano (Greece). J. Volcanol. Geotherm. Res. 387, 106666 https://doi.org/10.1016/j.jvolgeores.2019.106666.

Popa, R.G., Dietrich, V.J., Bachmann, O., 2020. Effusive-explosive transitions of water-undersaturated magmas. The case study of Methana Volcano, South Aegean Arc. J. Volcanol. Geotherm. Res. 399, 106884 https://doi.org/10.1016/j.jvolgeores.2020.106884.

Rabillard, A., Jolivet, L., Arbaret, L., Bessière, E., Laurent, V., Menant, A., et al., 2018. Synextensional Granitoids and Detachment Systems within Cycladic Metamorphic Core Complexes (Aegean Sea, Greece): toward a Regional Tectonomagmatic Model. Tectonics 37 (8), 2328–2362. https://doi.org/10.1029/2017TC004697.

Ranjan, P., Konstantinou, K.I., 2020. Mapping Intrinsic and Scattering Attenuation in the Southern Aegean Crust using S Wave Envelope Inversion and Sensitivity Kernels Derived from Perturbation Theory. J. Geophys. Res. Solid Earth 125 (10). https://doi.org/10.1029/2020JB020821 e2020JB020821.

Ranjan, P., Konstantinou, K.I., Andinisari, R., 2019. Spatial distribution of Random Velocity Inhomogeneities in the Southern Aegean from Inversion of S Wave Peak Delay Times. J. Geophys. Res. Solid Earth 124 (10), 10393–10412. https://doi.org/10.1029/2018JB017198.

Rawlinson, N., Spakman, W., 2016. On the use of sensitivity tests in seismic tomography. Geophys. J. Int. 205 (2), 1221–1243. https://doi.org/10.1093/gji/ggw084.

Reilinger, R., McClusky, S., Vernant, P., Lawrence, S., Ergintav, S., Cakmak, R., et al., 2006. GPS constraints on continental deformation in the Africa-Arabia-Eurasia continental collision zone and implications for the dynamics of plate interactions. J. Geophys. Res. Solid Earth 111, B05411. https://doi.org/10.1029/2005JB004051.

Reilinger, R., McClusky, S., Paradissis, D., Ergintav, S., Vernant, P., 2010. Geodetic constraints on the tectonic evolution of the Aegean region and strain accumulation along the Hellenic subduction zone. Tectonophysics 488 (1–4), 22–30. https://doi.org/10.1016/J.TECTO.2009.05.027.

Ring, U., Glodny, J., Will, T., Thomson, S., 2010. The Hellenic Subduction System: High-Pressure Metamorphism, Exhumation, Normal Faulting, and Large-Scale Extension. https://doi.org/10.1146/annurev.earth.050708.170910.

Ruscic, M., Bocchini, G.M., Becker, D., Meier, T., van Keken, P.E., 2019. Variable spatio-temporal clustering of microseismicity in the Hellenic Subduction Zone as possible indicator for fluid migration. Lithos 346–347, 105154. https://doi.org/10.1016/j.lithos.2019.105154.

Saltogianni, V., Gianniou, M., Taymaz, T., Yolsal-Çevikbilen, S., Stiros, S., 2015. Fault slip source models for the 2014 M_w 6.9 Samothraki-Gökçeada earthquake (North Aegean Trough) combining geodetic and seismological observations. J. Geophys. Res. Solid Earth 120 (12), 8610–8622. https://doi.org/10.1002/2015JB012052.

Sector For Seismology, I.O.H., 1982. Montenegrin seismic network. In: Sector for Seismology, Institute of Hydrometeorology and Seismology of Montenegro. https://doi.org/10.7914/SN/ME.

Sevostianov, I., 2020. Gassmann equation and replacement relations in micromechanics: a review. Int. J. Eng. Sci. https://doi.org/10.1016/j.ijengsci.2020.103344. Elsevier Ltd.

Shaw, B., Jackson, J., 2010. Earthquake mechanisms and active tectonics of the Hellenic subduction zone. Geophys. J. Int. 181 (2), 966–984. https://doi.org/10.1111/j.1365-246X.2010.04551.x.

Sodoudi, F., Kind, R., Hatzfeld, D., Priestley, K., Hanka, W., Wylegalla, K., et al., 2006. Lithospheric structure of the Aegean obtained from P and S receiver functions. J. Geophys. Res. Solid Earth 111 (B12). https://doi.org/10.1029/2005JB003932 n/a-n/a.

Sokos, E., Zahradník, J., Gallovič, F., Serpetsidaki, A., Plicka, V., Kiratzi, A., 2016. Asperity break after 12 years: the M_w6.4 2015 Lefkada (Greece) earthquake. Geophys. Res. Lett. 43, 6137–6145. https://doi.org/10.1002/2016GL069427.

Spakman, W., Wortel, M.J.R., Vlaar, N.J., 1988. The Hellenic Subduction Zone: a tomographic image and its geodynamic implications. Geophys. Res. Lett. 15 (1), 60–63. https://doi.org/10.1029/GL015i001p00060.

Strobl, M., Hetzel, R., Fassoulas, C., Kubik, P.W., 2014. A long-term rock uplift rate for eastern Crete and geodynamic implications for the Hellenic subduction zone. J. Geodyn. 78, 21–31. https://doi.org/10.1016/j.jog.2014.04.002.

Suckale, J., Rondenay, S., Sachpazi, M., Charalampakis, M., Hosa, A., Royden, L.H., 2009. High-resolution seismic imaging of the western Hellenic subduction zone using teleseismic scattered waves. Geophys. J. Int. 178 (2), 775–791. https://doi.org/10.1111/j.1365-246X.2009.04170.x.

Technological Educational Institute of Crete, 2006. Seismological Network of Crete. International Federation of Digital Seismograph Networks. https://doi.org/10.7914/SN/HC.

Tirel, C., Brun, J.P., Burov, E., Wortel, M.J.R., Lebedev, S., 2013. A plate tectonics oddity: Caterpillar-walk exhumation of subducted continental crust. Geology 41 (5), 555–558. https://doi.org/10.1130/G33862.1.

Toyokuni, G., Zhao, D., Chen, K.H., 2021. Structural control on the 2018 and 2019 Hualien earthquakes in Taiwan. Phys. Earth Planet. Inter. 312, 106673 https://doi.org/10.1016/j.pepi.2021.106673.

Um, J., Thurber, C., 1987. A fast algorithm for two-point seismic ray tracing. Bull. Seismol. Soc. Am. 77 (3), 972–986.

University of Athens, 2008. University of Athens, Seismological Laboratory. International Federation of Digital Seismograph Networks. https://doi.org/10.7914/SN/HA.

University of Patras, G.D., 2000. PSLNET, Permanent Seismic Network Operated by the University of Patras. International Federation of Digital Seismograph Networks, Greece. https://doi.org/10.7914/SN/HP.

van Hinsbergen, D.J.J., Hafkenscheid, E., Spakman, W., Meulenkamp, J.E., Wortel, R., 2005. Nappe stacking resulting from subduction of oceanic and continental lithosphere below Greece. Geology 33 (4), 325–328. https://doi.org/10.1130/G20878.1.

Ventouzi, C., Papazachos, C., Hatzidimitriou, P., Papaioannou, C., 2018. Anelastic P- and S- upper mantle attenuation tomography of the southern Aegean Sea subduction area (Hellenic Arc) using intermediate-depth earthquake data. Geophys. J. Int. 215 (1), 635–658. https://doi.org/10.1093/gji/ggy292.

Wang, H., Zhao, D., Huang, Z., Xu, M., Wang, L., Nishizono, Y., Inakura, H., 2018. Crustal tomography of the 2016 Kumamoto earthquake area in West Japan using P and PmP data. Geophys. J. Int. 214 (2), 1151–1163. https://doi.org/10.1093/gji/ggy177.

Watkins, W.D., Thurber, C.H., Abbott, E.R., Brudzinski, M.R., 2018. Local earthquake tomography of the Jalisco, Mexico region. Tectonophysics 724–725, 51–64. https://doi.org/10.1016/j.tecto.2018.01.002.

Wei, W., Zhao, D., Wei, F., Bai, X., Xu, J., 2019. Mantle dynamics of the Eastern Mediterranean and Middle East: Constraints from P-wave anisotropic tomography. Geochem. Geophys. Geosyst. 20 (10), 4505–4530. https://doi.org/10.1029/2019GC008512.

Wessel, P., Luis, J.F., Uieda, L., Scharroo, R., Wobbe, F., Smith, W.H.F., Tian, D., 2019. The generic mapping tools version 6. Geochem. Geophys. Geosyst. 20 (11), 5556–5564. https://doi.org/10.1029/2019GC008515.

Zhao, D., Kanamori, H., Negishi, H., Wiens, D., 1996. Tomography of the source area of the 1995 Kobe earthquake: evidence for fluids at the hypocenter? Science 274 (5294), 1891–1894. https://doi.org/10.1126/science.274.5294.1891.